Mechanisms of interaction between stationary crossflow instabilities and forward-facing steps

Casacuberta Puig, J.; Hickel, S.; Kotsonis, M.

DOI
10.2514/6.2021-0854

Publication date
2021

Document Version
Final published version

Published in
AIAA Scitech 2021 Forum

AIAA SciTech Forum
11–15 & 19–21 January 2021, VIRTUAL EVENT
AIAA Scitech 2021 Forum

10.2514/6.2021-0854

Mechanisms of interaction between stationary crossflow instabilities and forward-facing steps

J. Casacuberta*, S. Hickel †, and M. Kotsonis‡
Delft University of Technology, Delft, The Netherlands, 2629HS

We study the interaction between a stationary crossflow instability and forward-facing steps in a swept-wing boundary layer using Direct Numerical Simulations (DNS). The stationary primary crossflow mode is imposed at the inflow. Steps of several heights are modeled. Particular emphasis is placed on ensuring a fully stationary solution, in order to isolate the modulation of the primary instability at the step and the generation of stationary secondary perturbations. The main features of the base flow are step-induced flow reversal and secondary inflection points. When approaching the step, the incoming crossflow instability lifts up and passes over it. Additional perturbation streaks arise, which are accompanied by secondary stationary vortices that have the same spanwise wavenumber as the fundamental crossflow disturbance. For sufficiently high steps, secondary perturbation structures attain amplitude values comparable in magnitude to primary instability in the vicinity of the step. We propose metrics to quantify the impact of the step on the development of the crossflow disturbance upon interaction. Considering energy-based criteria, we find that the crossflow perturbation is amplified upstream of the step. Interestingly, the incoming primary crossflow instability undergoes strong stabilization immediately downstream of the largest step. The mechanisms revealed in this work provide a first insight into the possible causes of transition on swept wings due to forward-facing steps.

Nomenclature

$(\cdot)_b$	=	base flow variable
$(\cdot)'$	=	perturbation variable measured from the base flow
$(\cdot)'_{(0,j)}$	=	jth stationary perturbation spatial modal component
$\{u, v, w\}$	=	flat-plate-oriented velocity field
$\{u_s, v_s, w_s\}$	=	inviscid-streamline-oriented velocity field
u_∞	=	inflow free-stream streamwise velocity
w_∞	=	free-stream spanwise velocity
u_e	=	free-stream streamwise velocity
$\hat{u}_e$	=	*pseudo*-free-stream streamwise velocity
δ_0	=	inflow boundary layer thickness
λ_z	=	spanwise wavelength of the fundamental crossflow instability
β_0	=	spanwise wavenumber of the fundamental crossflow instability
α_i	=	streamwise perturbation growth rate
$A_{(0,j)}$	=	amplitude of the jth perturbation Fourier mode
$\lvert\tilde{\cdot}\rvert_{(0,j)}$	=	shape function of the jth perturbation Fourier mode
h	=	step height
$\{x, y, z\}$	=	flat-plate-oriented spatial coordinates
$\{x_s, y_s, z_s\}$	=	inviscid-streamline-oriented spatial coordinates
x_{st}	=	flat-plate-oriented streamwise coordinate with origin at the step location

*PhD Candidate, Section of Aerodynamics, Faculty of Aerospace Engineering, Correspondence: J.CasacubertaPuig@tudelft.nl
†Full Professor, Section of Aerodynamics, Faculty of Aerospace Engineering
‡Associate Professor, Section of Aerodynamics, Faculty of Aerospace Engineering

I. Introduction

The reduction of drag on the swept wings of subsonic aicraft is of concern for commercial aviation due to the major economical and environmental impact involving noise and air pollution. Laminar Flow Control (LFC) techniques have demonstrated high potential to delay laminar-turbulent transition and hence reduce skin friction drag by controlling the growth of boundary layer instabilities [1]. However, despite promising results from a theoretical basis and in laboratory testing, laminar flow is difficult to achieve in practice [2]. The effectiveness of LFC techniques in an operational environment is severely affected by the presence of geometrical imperfections, which arise from either environmental factors (i.e., debris, insect strikes, fowling, etc.) or due to manufacturing tolerances. Prominent in the leading edge area of wings are two-dimensional spanwise imperfections in the form of steps at the junctions between panels or in the leading edge-to-wing box [3]. The ability to exploit LFC and to achieve fully laminar wings in *realistic* flight conditions invokes the necessity to understand the interaction between pre-existing boundary layer instabilities and step-like roughness. In our work, the focus is put on forward-facing step geometries.

The earliest studies on laminar-turbulent transition induced by steps in two-dimensional boundary layers did not include the effect of external pressure gradients. Considering wing flows, Drake et al. [4] carried out pioneering experimental work involving steps mounted on unswept surfaces featuring a pressure gradient. They proposed correlations of the movement of the transition front and the roughness Reynolds number

$$Re_{hh} = \frac{u_h h}{\nu_h}, \tag{1}$$

where h is the roughness height and u_h, ν_h are the velocity and viscosity of the undisturbed boundary layer at the step height. *Small* steps were initially tested, for which the transition process showed to be insensitive. The height was then increased gradually until the step started to affect transition significantly and to move the transition front upstream. The height was kept increasing until the transition front reached the immediate vicinity of the step.

Duncan Jr. et al. [5] used data from infrared thermography measurements in in-flight tests to carry out an analysis in a fashion similar to Drake et al. [4]. However, as opposed to Drake et al. [4], besides the effect of pressure gradient, Duncan Jr. et al. [5] included the effect of the sweep angle as well. They reported values of the critical roughness Reynolds number, i.e., the value of Re_{hh} above which the step starts to move the transition front upstream, significantly lower than Drake et al. [4]. Three-dimensional boundary layers feature different stability characteristics than two-dimensional boundary layers in this context. When considering swept-wing flows, the combined effect of sweep angle and external streamwise pressure gradient causes the inviscid streamlines to bend inward. Whereas the pressure force and the centrifugal force balance each other in fluid parcels in the inviscid flow region far from the wall, an imbalance between these two forces exists in the boundary layer where viscous effects are significant. As a consequence, a secondary flow, the so-called crossflow, is induced in the boundary layer region. Particularly relevant for the study of boundary layer disturbances is the velocity profile projected in the plane whose normal locally points in the direction tangent to the inviscid streamline. Such velocity component must vanish at the wall and when approaching the outer flow region, inasmuch as it is orthogonal to the direction of the inviscid streamline. Hence, it must contain an inflection point. The latter gives rise to a strong inviscid instability mechanism, the crossflow instability, which may be of travelling or stationary nature. Within the scope of the current work, the focus is put on the stationary crossflow instability. It is the dominant kind in environments with low free-stream turbulence levels such as free flight.

Duncan Jr. et al. [6] extended the analysis of Duncan Jr. et al. [5] with experimental work carried out in a low-disturbance wind tunnel. For all step heights tested, the disturbance amplification factor, N, was found to increase immediately downstream of the step. Through hotwire measurements, Duncan Jr. et al. [6] observed that for critical step heights, forward-facing steps strongly amplify the stationary crossflow instability, whereas little effect on the unsteady disturbance content was produced.

Tufts et al. [2] studied numerically the interaction between an incoming stationary crossflow instability and forward-facing steps. The step-flow topology includes helical flow induced by two recirculation bubbles, one located in the lower step corner and one located immediately downstream of the step. In line with observations of Duncan Jr. et al. [6], Tufts et al. [2] captured strong amplification of the incoming stationary crossflow instability when passing over forward-facing steps with critical roughness heights. The interaction between the helical flow in the upper separation bubble and the incoming crossflow vortices was proposed as a possible mechanism to explain the amplification of the incoming disturbance. Moreover, Tufts et al. [2] observed a near-wall *lobe* in the disturbance shape at the step location. They reported that for *small* step cases, and when moving downstream of the step, the secondary disturbance peak decays in amplitude and eventually disappears, whereas for *large* step cases, the near-wall lobe grows and it appears to absorb the original lobe. Tufts et al. [2] indicated that the secondary perturbation lobe is located at the same wall-normal

position as the flow separation region, hence they suggested that decreasing the size of the upper separation bubble is a way to mitigate the effect of the step on the incoming perturbation. These results motivated Tufts et al. [2] to present a model of an either destructive or constructive interaction between the incoming stationary crossflow vortices and helical flow at the step.

Using naphthalene flow visualisation, Saeed et al. [7] investigated effects of the step location and observed that steps near the neutral point have the strongest effect on stationary disturbances. Rius-Vidales et al. [3] conducted an extensive experimental investigation using infrared thermography and reported the critical amplification factor reduction induced by the step, ΔN, to be affected by y_c/h and $h/\delta^\star$, the estimated crossflow vortex height-to-step height ratio and the relative step height respectively. Rius-Vidales et al. [3] found no evidence for universal validity of the criteria proposed by Tufts et al. [2]. In contrast, they identified a significantly more complex functional relationship that is affected not only by the topological characteristics of the incoming instability, but also by its respective amplitude, growth rate, and overall stability characteristics.

Eppink and Casper [8] performed PIV experiments and segregated relevant effects downstream of the step location; close to the step, flow separation and crossflow reversal were identified as main flow features. In this region, significant growth of stationary perturbations was captured. Further downstream, the so-called *flow-recovery region* is a second region of strong growth of the stationary perturbations, not necessarily at the same spanwise wavelengths which had undergone strong amplification near the step. This second amplification phase is partially ascribed to non-linear effects, inasmuch as significant sub-harmonic growth is measured in this region. Eppink and Casper [8] put into question the model presented by Tufts et al. [2] for determining critical step heights; they did not find evidence of constructive interaction between the incoming crossflow vortices and the step-induced helical flow.

While the majority of numerical investigations of transitional flows over geometrical imperfections is performed using Direct Numerical Simulations, other methodologies have been emerging in recent years. Sumariva and Hein [9] used the Linearised Harmonic Navier Stokes equations (LHNS) to study the impact of isolated humps on convective Tollmien-Schlichting (TS) instabilities. Cooke et al. [10] applied the LHNS approach to DNS base flows to investigate stationary crossflow perturbations interacting with step excrescence. When considering forward-facing steps, LHNS was proven to be capable of dealing with the rapid streamwise variations of the base flow near the step. Cooke et al. [10] reported sudden stationary crossflow growth triggered by the step corner. In line with results of Tufts et al. [2] and Eppink and Casper [8], Cooke et al. [10] identified a secondary peak in the stationary perturbation shape emerging at the step location near the wall, which merges back with the primary peak as the perturbation structure moves further downstream. While Tufts et al. [2] attributed the growth of the secondary peak to the interaction between the incoming disturbance and the upper region of flow reversal, Cooke et al. [10] did not capture an upper separation bubble –despite their step geometries to reach up to 53% of the boundary layer thickness–. Based on this Cooke et al. [10] question the conclusions of Tufts et al. [2] with regard to the role of the upper separation bubble in amplifying the incoming perturbation.

There is controversy in the literature with regard to the role played by step-induced flow features in altering the evolution of the pre-existing disturbance. In some cases, it has lead to conflicting hypotheses. Furthermore, to quantitatively characterize the impact of the step on the stability properties of the incoming stationary perturbation upon interaction remains an open problem. We contribute to the discussion by performing Direct Numerical Simulations (DNS) of the base flow and the steady-state flow solution that arises from the interaction between the three-dimensional instability and the step. We assess the organization of the stationary perturbation structures near the step and analyze step-induced flow structures and mechanisms with potential to modify the behaviour of the pre-existing disturbance. Particular emphasis is placed on characterizing the effect of the step on the incoming stationary instability solely, disregarding possible effects on the unsteady perturbation content. For this purpose, we do not trigger unsteady disturbances which are inherent to experimental environments; our intention is to isolate and shed light onto relevant flow mechanisms which could be partially masked in more complex unsteady flow environments.

The organization of the paper is as follows. In section II, the flow problem is defined and we introduce the setup characteristics, the main notation, and the numerical setup of our DNS. We start the discussion of the results in section III, containing a qualitative description of the perturbation evolution in the smooth case, the step-distorted base flow topology, and the organization of primary and secondary perturbation structures in the near-step regime. In section IV, we quantify the effect of the step on the stability characteristics of the pre-existing crossflow disturbance upon interaction.

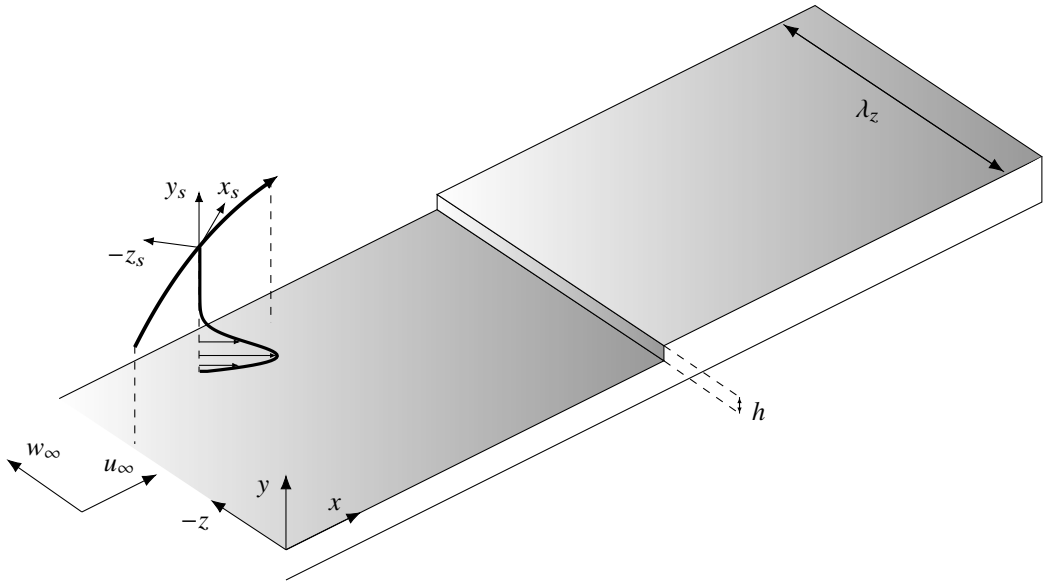

Figure 1 Sketch of the flow problem: flat plate and step geometry, external inviscid streamline with associated crossflow velocity profile, flat-plate-aligned coordinate system (x, y, z), inviscid streamline-aligned coordinate system (x_s, y_s, z_s), free-stream velocity components, u_∞ and w_∞, step height, h, and spanwise domain length, λ_z.

II. Methodology

A. Flow problem and geometry

A sketch of the flow problem is depicted in Fig. 1. We model the swept-wing flow as flow over a swept flat plate with a prescribed favourable pressure gradient aligned with the streamwise direction. The evolution of external pressure, p_e, resembles the airfoil-induced streamwise pressure gradient near the leading edge of a swept wing. For this purpose, we use data acquired during independent experiments performed at TU Delft for a sweep angle of 45°. See Rius-Vidales et al. [3] for details on the wing set-up employed in the experimental campaign. The computational domain and the main coordinate system $\mathbf{x} = [x\ y\ z]^T$ are correspondingly swept and aligned with the leading edge of the airfoil. A laminar three-dimensional boundary layer superimposed with a small-amplitude crossflow disturbance with a shape function obtained by linear stability analysis is introduced at the inflow. The boundary layer and the perturbation develop over the flat plate in the x direction and encounter a forward-facing step distributed along the spanwise direction, z. The direction normal to the wall is denoted by y and the height of the step by h. To account for the sweep angle, the incoming free-stream velocity is composed of a velocity component in x-direction, u_∞, and a velocity component in z-direction, w_∞. The inflow boundary layer thickness, $\delta_0 = 7.71 \times 10^{-4}$ m, and the inflow free-stream streamwise velocity, $u_\infty = 15.10$ m/s, have been chosen as global characteristic quantities of our flow problem.

DNS for three different forward-facing step heights at a fixed streamwise location and for fixed free-stream properties have been performed. Table 1 shows a comparison between boundary layer properties and step properties among all tested configurations. The parameter $\delta_{99,h}$ expresses the undisturbed boundary layer thickness at the location where the steps would be placed, and we introduce the definition

$$Re_h = \frac{u_\infty h}{\nu_h}. \tag{2}$$

All tested configurations represent sub-boundary layer roughnesses; the largest step reaches approximately half of the undisturbed boundary layer thickness. To analyse the effect of the step location lies outside the scope of the current work. Thereby, the streamwise location of the step is fixed for all configurations, and corresponding to 20% of the chord of the wing model used to extract the free-stream conditions. The inlet of the numerical domain is virtually placed at 5% of the chord.

Case	h/δ_0	$h/\delta_{99,h}$	u_h/u_∞	Re_h	Re_{hh}
Step I	0.57	0.31	0.76	448.80	339.06
Step II	0.73	0.40	0.91	577.13	523.97
Step III	0.95	0.52	1.07	748.13	797.01

Table 1 Comparison of boundary layer parameters among step cases.

B. Coordinate systems, parameters, and notation

In this work two coordinate systems are employed, namely, the flat plate-aligned coordinate system, $\{x, y, z\}$, and a coordinate system whose axes are *locally* oriented based on the trajectory of the inviscid streamline, $\{x_s, y_s, z_s\}$. We denote by x_s the unit vector pointing in the direction locally tangent to the inviscid streamline, $y_s = y$, and z_s is orthonormal to x_s and y_s (Fig. 1). The velocity field in the flat-plate-aligned coordinate system is expressed as follows: the x-aligned velocity is indicated by u, while v and w respectively refer to the wall-normal and the spanwise velocity components.

Letting $\mathbf{q}$ be the state vector $\mathbf{q} = [u\ v\ w\ p]^T$, the developed flow is decomposed as

$$\mathbf{q}(\mathbf{x}) = \mathbf{q}_b(\mathbf{x}) + \mathbf{q}'(\mathbf{x}). \tag{3}$$

The left-hand-side (LHS) of Eq. 3 is the steady developed flow solution, $\mathbf{q}_b$ is the laminar base flow solution, $\mathbf{q}'$ is the stationary disturbance field, which both are functions of the spatial coordinate vector $\mathbf{x}$. The base flow is assumed to be a spanwise-invariant flow solution, i.e., $\partial \mathbf{q}_b/\partial z = 0$; under the hypothesis of infinite span wings, the spanwise external pressure gradient and the acceleration of the base flow in z are assumed negligible [11–13]. Accordingly, the free-stream spanwise velocity w_∞ is set constant throughout the domain and such that $w_\infty = -1.24u_\infty$.

Upstream of the step, the perturbation field is composed of the streamwise-developing crossflow disturbance and its associated sub-harmonics. The fundamental stationary crossflow disturbance, referred to as $(0, 1)$, is prescribed at the inflow, whereas the sub-harmonic components arise further downstream due to non-linear interactions. In this work we refer to instability waves as (m, n). The index $n = 2, 3, 4, \ldots$ expresses waves whose spanwise wavenumber is a multiple of the fundamental one, denoted by β_0. The index m expresses waves of unsteady nature, thus $m = 0$ within the scope of this work. The mean-flow distortion is denoted as $(0, 0)$. Upstream of the step, the stationary crossflow instability manifests in the developed flow field as stationary co-rotating vortices, whose axes of rotation are approximately aligned in the direction of the inviscid streamline. The instability itself, however, develops as counter-rotating vortices [14]. To model the streamwise evolution of the crossflow mode, periodic boundary conditions are applied at the spanwise boundaries, and the spanwise domain length is set equal to the spanwise wavelength of the fundamental wave, $\lambda_z = 2\pi/\beta_0$. In this work, we choose $\lambda_z = 7.5$ mm, which is the wavelength of the stationary crossflow mode with the largest amplification factor, as predicted by linear local stability methods applied to the computed DNS base flow. Despite their inherent parallel flow assumption [15], linear local methods can predict the wavelengths of the most amplified stationary crossflow disturbances [11].

The results of the DNS are Fourier analyzed in the spanwise direction. The perturbation field is decomposed as a sum of spatial Fourier modes, i.e.,

$$q'_k = \sum_{j=0}^{j=N} A^k_{(0,j)} |\tilde{q}^k|_{(0,j)} \mathrm{e}^{\mathrm{i}(\phi^k_{(0,j)} + j\beta_0 z)}, \tag{4}$$

where N is the total number of modes considered, k expresses the pertinent component of the state vector $\mathbf{q}$, $|\tilde{q}|_{(0,j)} = |\tilde{q}|_{(0,j)}(x, y) \in \mathbb{R}$ is the normalized shape function of Fourier mode $(0, j)$, $\phi_{(0,j)} = \phi_{(0,j)}(x, y) \in \mathbb{R}$ is the phase of Fourier mode $(0, j)$, $A_{(0,j)} = A_{(0,j)}(x) \in \mathbb{R}$ is the amplitude of Fourier mode $(0, j)$, and $\mathrm{i}^2 = -1$. The real and imaginary parts of Eq. 4 are expressed as $\mathrm{Re}\left\{q'_k\right\}$ and $\mathrm{Im}\left\{q'_k\right\}$ respectively.

C. Free-stream characterization and crossflow decomposition

The external free-stream velocity u_e increases in x. This is a consequence of the fact that a favourable pressure gradient is prescribed. Moreover, as the pressure gradient is not constant in our DNS case, du_e/dy is non-negligible, and thus $u_e = u_e(x, y)$ with $du_e/dx \gg du_e/dy$. The free-stream non-uniformity in y poses the challenge of establishing

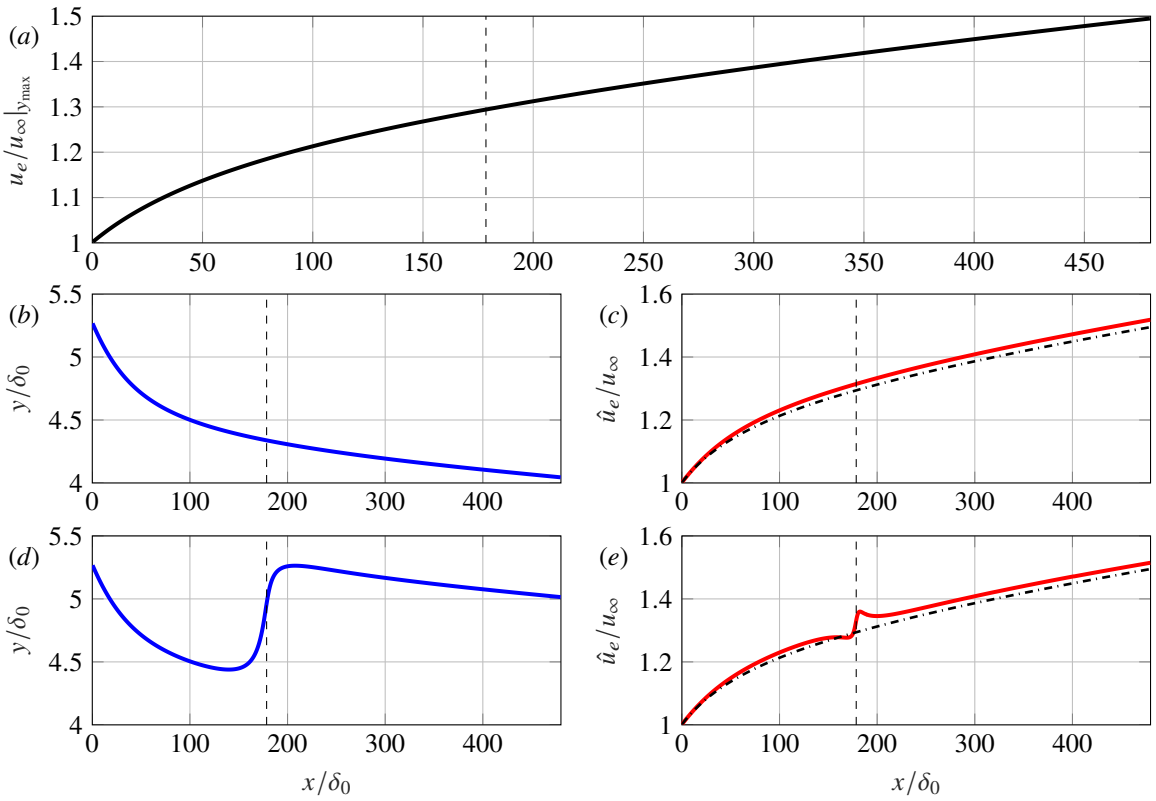

Figure 2 Streamwise evolution of free-stream properties: streamwise velocity at the upper boundary (*a*), inflow streamline used to define the *pseudo*-free-stream in the clean case (*b*) and in step case III (*d*), streamwise velocity of the *pseudo*-free-stream in the clean case (solid red) (*c*) and in step case III (solid red) (*e*). Streamwise location of the step (black dashed), trend shown in (*a*) replicated in (*c*, *e*) (black dash-dotted).

a robust definition of *pseudo*-free-stream conditions to be employed for the characterization of boundary layer properties. By *pseudo*-free-stream, we mean a unique definition of free-stream properties for all step cases, which is representative for the outer-flow evolution and is a function of x only. For this purpose, we numerically integrate an inflow streamline forward in the streamwise direction. For all smooth and step cases, the properties of the flow along the trajectory of each integrated streamline define their respective *pseudo*-free-stream properties. Hereafter, we denote by $\hat{u}_e = \hat{u}_e(x)$ the (external) streamwise velocity associated to the *pseudo*-free-stream. Figure 2 portrays the trajectories of integrated streamlines and the evolution of $\hat{u}_e$ in x for the clean and the largest step cases.

A robust definition of representative free-stream properties is also required to perform the crossflow-velocity decomposition, that is, to express the velocity components in the coordinate system oriented with respect to the local deflection of the characteristic inviscid streamline. Accordingly, we evaluate the angle that x_s forms with x as

$$\varphi(x) = \arctan\left(\frac{w_\infty}{\hat{u}_e(x)}\right), \tag{5}$$

and the base flow velocity components in the direction tangent, $u_{b,s}$, and orthogonal, $w_{b,s}$, to the characteristic inviscid streamline are expressed as

$$\begin{aligned} u_{b,s} &= u_b \cos(\varphi) + w_b \sin(\varphi), \\ w_{b,s} &= w_b \cos(\varphi) - u_b \sin(\varphi), \end{aligned} \tag{6}$$

while $v_{b,s} = v_b$. In a similar fashion, the real part of the flat-plate-aligned velocity perturbation field $(0, 1)$ –as defined in Eq. 4– projected on the inviscid-streamline-aligned coordinate system reads

$$
\begin{aligned}
\mathrm{Re}\left\{u'_{s,(0,1)}\right\} &= \mathrm{Re}\left\{u'_{(0,1)}\right\}\cos(\varphi) + \mathrm{Re}\left\{w'_{(0,1)}\right\}\sin(\varphi),\\
\mathrm{Re}\left\{v'_{s,(0,1)}\right\} &= \mathrm{Re}\left\{v'_{(0,1)}\right\},\\
\mathrm{Re}\left\{w'_{s,(0,1)}\right\} &= \mathrm{Re}\left\{w'_{(0,1)}\right\}\cos(\varphi) - \mathrm{Re}\left\{u'_{(0,1)}\right\}\sin(\varphi).
\end{aligned}
\tag{7}
$$

Hereafter, a subindex "s" expresses that the velocity components are expressed on the streamline-based coordinate system.

D. Computational setup

We compute the step-flow field by numerically solving the incompressible Navier-Stokes equations. We perform independent DNS of the unperturbed laminar base flow and the stationary developed flow over the step. The stationary developed flow arises from the interaction between an incoming stationary crossflow instability and the step. In absence of unsteady perturbations, the DNS capture only perturbation mechanisms of stationary nature.

The DNS of the base flow and the developed flow are performed with INCA, a conservative finite-volume solver [16, 17]. Relevant previous applications of this flow solver include perturbation growth flow mechanisms in incompressible and compressible boundary layers. See for instance Hu et al. [18], who model the dynamics of a supersonic transitional flow over a backward-facing step, or Casacuberta et al. [19], who studied the transitional wake of a micro-ramp immersed in a quasi incompressible boundary layer. The incompressible Navier-Stokes equations are marched in time with a third-order Runge-Kutta method. A fifth-order upwind scheme is used to discretize the convective terms. We use the L_2-norm of the temporal derivatives, $\epsilon = 10^{-6}$ and $\epsilon = 10^{-9}$, as convergence criterion for the developed flow and base flow simulations, respectively. The time-converged base flow solutions are used as initial condition for the developed flow computations.

The flow problem is solved in a numerical domain of dimensions $0 \leq x/\delta_0 \leq 480$ in the streamwise direction, $0 \leq y/\delta_0 \leq 26$ in the wall-normal direction, and $-4.86 \leq z/\delta_0 \leq 4.86$ in the spanwise direction. For all configurations tested, the step is located at $x/\delta_0 = 178.56$. The coordinate $x_{\mathrm{st}} = x - 178.56\delta_0$, expresses the relative streamwise distance from the step. The streamwise domain length of the current set-up ensures that the evolution of the stationary perturbations and their harmonics are well captured. Furthermore, we place the upper boundary of our numerical domain sufficiently far from the wall, such that the influence of the step on the free-stream evolution near the top becomes negligible. This is a point of special attention, inasmuch as the independent empirical data used to define the top boundary condition of the DNS of the step cases was measured in a *smooth* wing configuration, i.e., without steps.

The results presented in this paper have been obtained with a computational grid containing 4×10^5 and 7.4×10^6 grid cells for the base flow and the developed flow cases respectively. Figure 3 portrays the structure of the grid around the step. The grid is homogeneous in the spanwise direction, with 2 and 18 grid cells along z for the base flow and the developed flow computations, respectively. The cells within a localized rectangular domain encompassing the near-step region are square-shaped. Further away from the region of interest, we coarsen the grid in both the streamwise and the wall-normal directions; hyperbolic stretching refinement is applied in the buffer region separating the near-step domain and the outer domain.

As boundary conditions, we prescribe total pressure at the outlet, whereas a static pressure distribution obtained from the independent empirical data is imposed at the top boundary. Velocity is extrapolated in a way that velocity

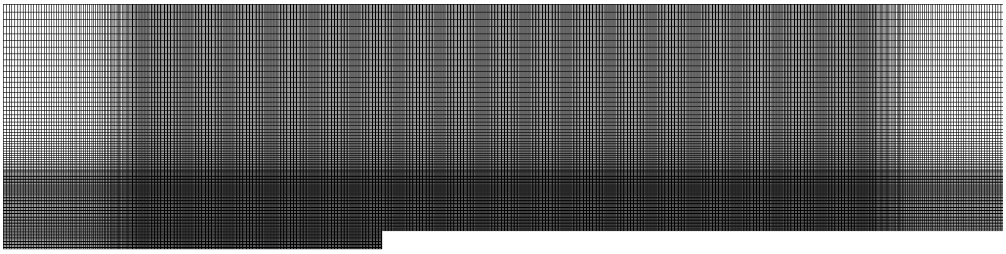

Figure 3 Grid structure around the step.

fluctuations are damped at the upper boundary [17]. To reproduce the experimental free-stream conditions described previously in our numerical simulations, we fit a polynomial of order four and with logarithmic basis to the experimental streamwise velocity distribution:

$$u_e^{\mathrm{exp}}/u_\infty = 0.0023\ln^4(x+c) + 0.0377\ln^3(x+c) + 0.1752\ln^2(x+c) + 0.5303\ln(x+c) + 1.8574, \tag{8}$$

with $c = 0.0468$ m. We use Eq. 8 and the assumption of irrotational flow in the outer flow region to compute a static pressure distribution that is prescribed as upper boundary condition in the DNS.

We apply periodic boundary conditions in the z direction and the no-slip condition at the wall. The three-dimensional laminar boundary layer at the inflow is obtained as the solution to the Falkner-Skan-Cooke equations [15], which we denote by u^{FSC}. For the DNS of the developed flow, we additionally perturb the inflow solution by adding a small-amplitude neutral stationary crossflow mode. Accordingly, the prescribed inflow streamwise velocity, u^{in}, reads

$$u^{\mathrm{in}} = u^{\mathrm{FSC}} + A_0\left(\tilde{u}_r^{\mathrm{in}}\left\{\cos(\alpha_r^{\mathrm{in}}x + \beta_0 z)\right\} - \tilde{u}_i^{\mathrm{in}}\left\{\sin(\alpha_r^{\mathrm{in}}x + \beta_0 z)\right\}\right), \tag{9}$$

in the developed flow simulations, whereas we impose $u^{\mathrm{in}} = u^{\mathrm{FSC}}$ in the base flow computations.

In Eq. 9, $\alpha_r^{\mathrm{in}} \in \mathbb{R}$ is the streamwise wavenumber of the inflow perturbation, $\tilde{u}^{\mathrm{in}} = \tilde{u}_r^{\mathrm{in}} + \mathrm{i}\tilde{u}_{\mathrm{i}}^{\mathrm{in}}$ is the normalized streamwise-velocity shape function of the inflow perturbation with $\max\left\{\mathrm{abs}(\tilde{u}^{\mathrm{in}})\right\} = 1$, and $A_0 \in \mathbb{R}$ is the initial disturbance amplitude. We impose $A_0 = 3.5\times10^{-3}u_\infty$ in the smooth and all step cases; the justification for this particular choice is given in section III.A. The values of α_r^{in}, $\tilde{u}_r^{\mathrm{in}}$, $\tilde{u}_i^{\mathrm{in}}$ used in Eq. 9 are the eigenproperties of the stationary crossflow mode obtained as the solution to a local linear Orr-Sommerfeld analysis [15] on the inflow DNS base flow profile.

III. Organization of the base flow and the perturbation field at the step

A. Perturbation development in the smooth case

We start the analysis of the results by describing the evolution of the perturbation field in the smooth flat plate. When analyzing the behaviour of the crossflow disturbance in further sections, differences in amplitude and perturbation shape distortion will be attributed to the presence of steps.

The laminar boundary layer and the small-amplitude crossflow mode imposed at the inflow develop along the flat plate. The boundary layer, which is invariant in the spanwise direction, grows in x. At the virtual location of the step, the boundary layer thickness has increased by 1.8 times. Figure 4 depicts the perturbation shape of the streamwise-velocity-perturbation Fourier modes $(0,1)$ and $(0,2)$. In the case of the fundamental component, the shape function displays a single-peak structure; the second harmonic is characterized by a double-peak structure.

We quantify the amplitude evolution in x of the different Fourier components by measuring amplitude at the wall-normal location of the global maxima of their respective shape functions, following the definition given in Eq. 4.

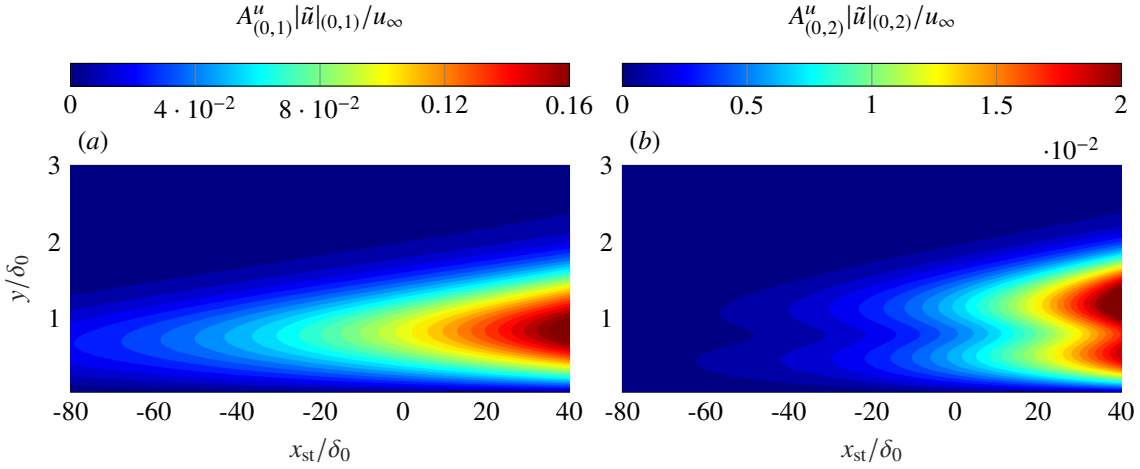

Figure 4 Shape of the streamwise-velocity-perturbation Fourier modes $(0,1)$ **(*a*) and** $(0,2)$ **(*b*).**

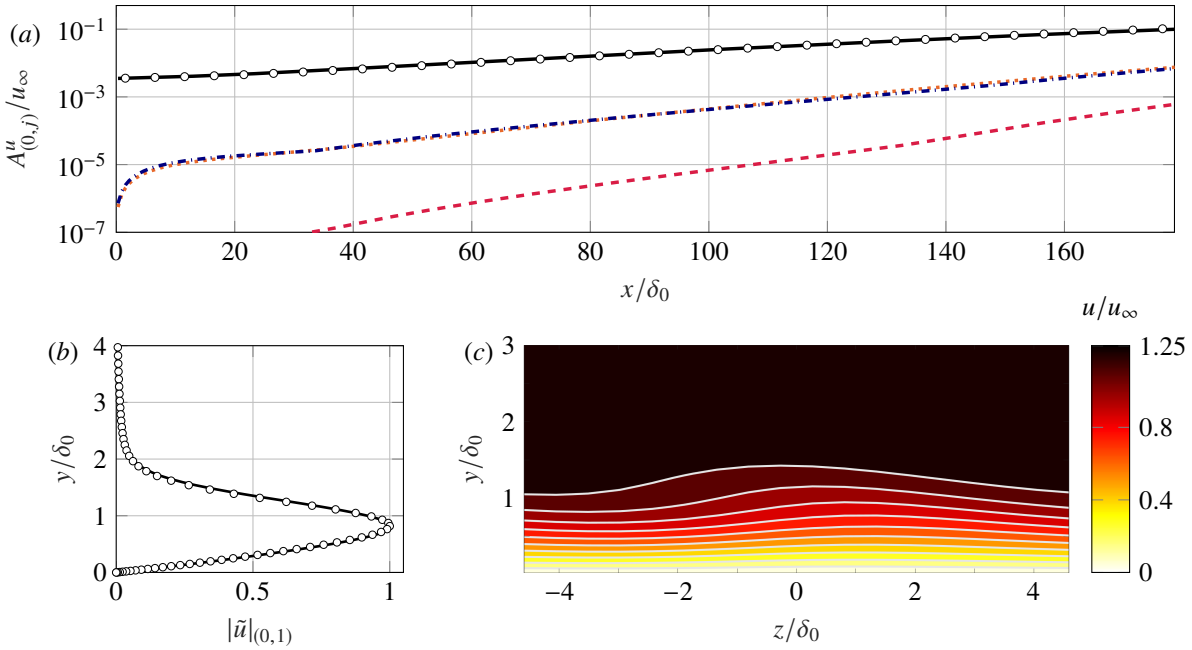

Figure 5 Streamwise evolution of the amplitude of the streamwise-velocity-perturbation Fourier modes $(0,0)$ **(dotted orange),** $(0,1)$ **(solid black),** $(0,2)$ **(dash-dotted blue),** $(0,3)$ **(dashed red) from DNS and from PSE (circles) (*a*). Shape function of the primary crossflow disturbance at** $x_{\text{st}} = 0$ **from DNS (solid black) and PSE (circles) (*b*). Plane of streamwise velocity in the developed flow field at** $x_{\text{st}} = 0$ **(*c*).**

We choose an inflow amplitude of the primary crossflow disturbance of $A_0 = 3.5 \times 10^{-3} u_\infty$. This choice yields exponential streamwise growth of the fundamental component until approximately the virtual location of the step, while the high-order harmonics are weakly activated at $x_{\text{st}} = 0$. By *weak* harmonics, we mean crossflow sub-harmonic waves whose amplitudes are orders of magnitude lower than the primary wave, and they do not significantly distort the base flow nor significantly deviate the streamwise evolution of the fundamental instability from the trend predicted by linear stability methods. This is illustrated in Fig. 5 (*a*) portraying the evolution in x of the amplitude of the fundamental and the sub-harmonic Fourier components. Figure 5 (*a*) additionally shows the amplitude evolution of the fundamental crossflow disturbance obtained by applying the Parabolized Stability Equations (PSE) approach [20] to the computed DNS base flow. We find good agreement with the trend measured from DNS. Significant differences between growth of the primary component in the DNS and from the linear stability method begins approximately downstream of the virtual location of the step. We also find agreement when comparing shape function profiles at $x_{\text{st}} = 0$, see Fig. 5 (*b*).

When the crossflow instability develops in x, the total developed flow field eventually displays a characteristic wavy pattern. This is shown in Fig. 5 (*c*) portraying the streamwise velocity of the field obtained as the superposition of the base flow and the full perturbation system at $x_{\text{st}} = 0$.

B. Topology of the base flow around the step

A major feature of the step-distorted laminar base flow is flow recirculation induced at the step, see Fig. 6 depicting streaklines of the base flow in the x-y plane. In this work, flow separation refers to the flat plate-aligned streamwise velocity, u_b. We capture flow reversal at the lower concave corner for all step configurations, as commonly reported in previous investigations [2, 10]. On the other hand, previous work debates the existence of flow recirculation downstream of the step. Whereas Tufts et al. [2] point out that an upper separation bubble is found for the whole range of step heights tested, Cooke et al. [10] do not capture flow reversal downstream of the step in any configuration –despite their steps reaching up to 53% of the undisturbed boundary layer thickness–. The results of our DNS show that flow separation in the upper corner is induced only in the largest step cases, i.e., step configurations II and III. The existence and the extent of flow recirculation has been further addressed by evaluating the distribution of wall shear. It ought to be mentioned, however, that a very weak and localized recirculation bubble cannot be excluded for step case I. Future computational

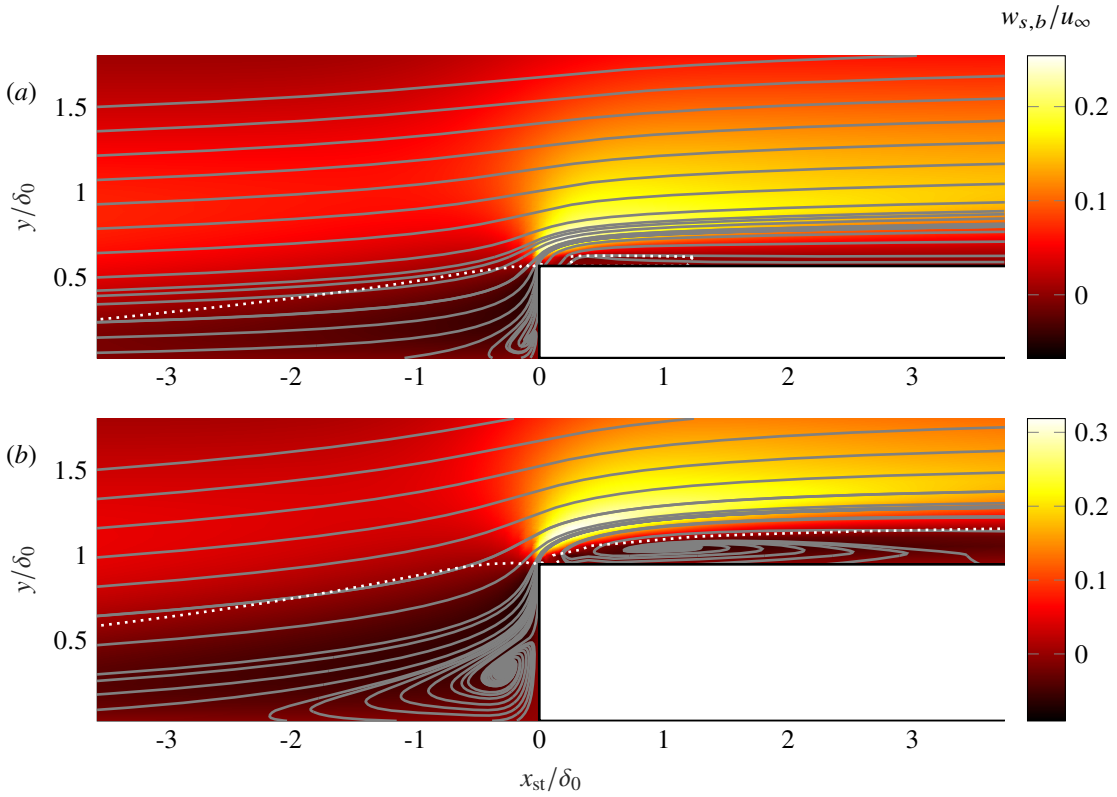

Figure 6 Base flow crossflow velocity, $w_{s,b}$, streaklines of the base flow field (u_b,v_b) (solid grey), loci of points with $w_{s,b} = 0$ (dotted white) for step case I (*a*), and step case III (*b*).

work involving more refined grids will shed light on this matter.

Table 2 summarizes the main features of the regions of flow separation induced upstream and downstream of the step. In this work, their basic geometrical properties are defined based on the evolution of $u_b = 0$. The region of flow recirculation at the lower step corner terminates at the step for all configurations, and the cores of their reverse flow vortices are maintained rather close to the step. Despite the increase in streamwise length of the flow separation region for an increase in step height, the magnitude of peak reversed-flow within is maintained rather low, never surpassing 1% of the local external velocity, $\hat{u}_e$, in any step case. The upper separation bubbles attain a higher strength, i.e., peak reversed-flow value, when compared to that at the lower corner; step cases II and III respectively acquire 1% and 3.3% of the local external velocity, $\hat{u}_e$.

Within the scope of classical pressure-induced laminar separation bubbles, Rodríguez et al. [21] indicate that a self-excited global mode exists in bubbles with peak reversed-flow values of at least 7% of the local free-stream velocity. Alam and Sandham [22] point out that an absolute instability mechanism may exist for bubbles with a strength of more than 15%. Notwithstanding that the separation bubbles observed in the present study are geometry-induced, the most critical bubble in our simulations is far from attaining the aforementioned values. Furthermore, our DNS of the stationary developed flow do not show evidence of the existence of a self-sustained global mode interacting with the incoming crossflow vortices.

Besides flow separation, we also capture reversal of the crossflow component in the near-step base-flow region. In the clean case, the combination of sweep angle and a favourable streamwise pressure gradient induces a crossflow component which is positive in our coordinate system. When a step is placed, it locally distorts the pressure distribution. When approaching the step in the x-direction, a local region of adverse pressure gradient is induced. In a very limited streamwise extent at the step corner, the pressure gradient momentarily becomes favourable, yet it is immediately followed in x by a second region of adverse pressure gradient. This behaviour is identical to that reported by Tufts et al. [2]. The two regions of adverse pressure gradient upstream and downstream of the step induce a negative crossflow

Feature	Property		Step I	Step II	Step III
Upstream	Start:	$x_{st}/\delta_0 =$	-0.59	-1.35	-2.81
separation	Height:	$y/\delta_0 =$	0.14	0.24	0.41
	Relative height:	$y/h =$	0.23	0.31	0.41
	Strength:	$-u_b/u_\infty =$	0.22×10^{-2}	0.50×10^{-2}	0.93×10^{-2}
	Relative strength:	$-u_b/\hat{u}_e =$	0.17×10^{-2}	0.38×10^{-2}	0.70×10^{-2}
Downstream	Start:	$x_{st}/\delta_0 =$	-	0.22	0.16
separation	End:	$x_{st}/\delta_0 =$	-	0.86	3.35
	Strength:	$-u_b/u_\infty =$	-	1.36×10^{-2}	4.39×10^{-2}
	Relative strength:	$-u_b/\hat{u}_e =$	-	1.03×10^{-2}	3.29×10^{-2}
Upstream	Start	$x_{st}/\delta_0 =$	-7.07	-9.51	-12.64
crossflow reversal	Strength:	$-w_{s,b}/u_\infty =$	5.77×10^{-2}	6.95×10^{-2}	7.55×10^{-2}
	Relative strength:	$-w_{s,b}/\hat{u}_e =$	4.38×10^{-2}	5.26×10^{-2}	5.69×10^{-2}
	Strength location:	$x_{st}/\delta_0 =$	corner	corner	corner
Downstream	Start:	$x_{st}/\delta_0 =$	0.27	0.22	0.16
crossflow reversal	End:	$x_{st}/\delta_0 =$	1.19	5.35	13.29
	Strength:	$-w_{s,b}/u_\infty =$	1.39×10^{-2}	3.65×10^{-2}	5.32×10^{-2}
	Relative strength:	$-w_{s,b}/\hat{u}_e =$	1.05×10^{-2}	2.75×10^{-2}	3.99×10^{-2}
	Strength location:	$x_{st}/\delta_0 =$	0.38	0.32	0.27

Table 2 Properties of the regions of flow separation and crossflow reversal at the step.

velocity near the wall. Downstream of the step, and further away from the wall, the crossflow component shows a strong (positive) increase, see Fig. 6. We capture crossflow reversal upstream and downstream of the step for all configurations. In contrast to the geometry-induced separation bubble(s), the crossflow reversal is a pressure-induced effect, carrying stronger history in the streamwise direction. As such, the regions of crossflow reversal span over a significantly larger streamwise extent than the areas of flow recirculation, see Table 2. Furthermore, the magnitude of the peak reversed-crossflow is generally larger (in absolute value) than the strength of the separation bubbles.

C. Organization of Fourier mode (0,1) in the near-step regime

A main question motivating the present study is the elucidation of the pertinent mechanisms governing the interaction of the incoming stationary crossflow instability with the forward-facing step. Therefore, we next put the focus on the perturbation organization in the immediate vicinity of the step and we first restrict the analysis to the primary Fourier mode. The evolution of the sub-harmonic content is discussed later on in section III.F.

The three-dimensional organization of the perturbation Fourier mode $(0, 1)$ near the step is portrayed in Fig. 7 ($u'_{(0,1)}$), and Fig. 22 in the Appendix ($w'_{(0,1)}$), at selected y-z planes. Additionally, Fig. 8 depicts the non-normalized shape function of the streamwise-velocity-perturbation Fourier mode $(0, 1)$ immediately upstream and downstream of the step. When the step is approached in x, the incoming instability gradually lifts up and passes over it. Figure 8 (*a.1-a.3*) illustrates that in the upstream vicinity of the step, the wall-normal position of the primary peak in the shape function has significantly shifted upward with respect to the smooth case. As the core of the incoming instability lifts up, a secondary peak in the shape function develops close to the wall. It manifests in the three-dimensional perturbation organization as a system of streaks alternating in the spanwise direction, see Fig. 7 and Fig. 22 in the Appendix. For all step heights, the primary peak –which is associated to the core of the pre-existing disturbance– remains after passing the step.

Downstream of $x_{st} = 0$ in step case I, Fourier mode $(0, 1)$ characterizes well the coherent evolution of the incoming instability and the mode shape qualitatively resembles that of the clean case. When considering step case III, however, the shape of Fourier mode $(0, 1)$ undergoes strong changes in topology, see Fig. 7 (*b*) and Fig. 22 (*b*) in the Appendix. The system of near-wall streaks captured upstream of the step arises downstream of the step as well. It develops

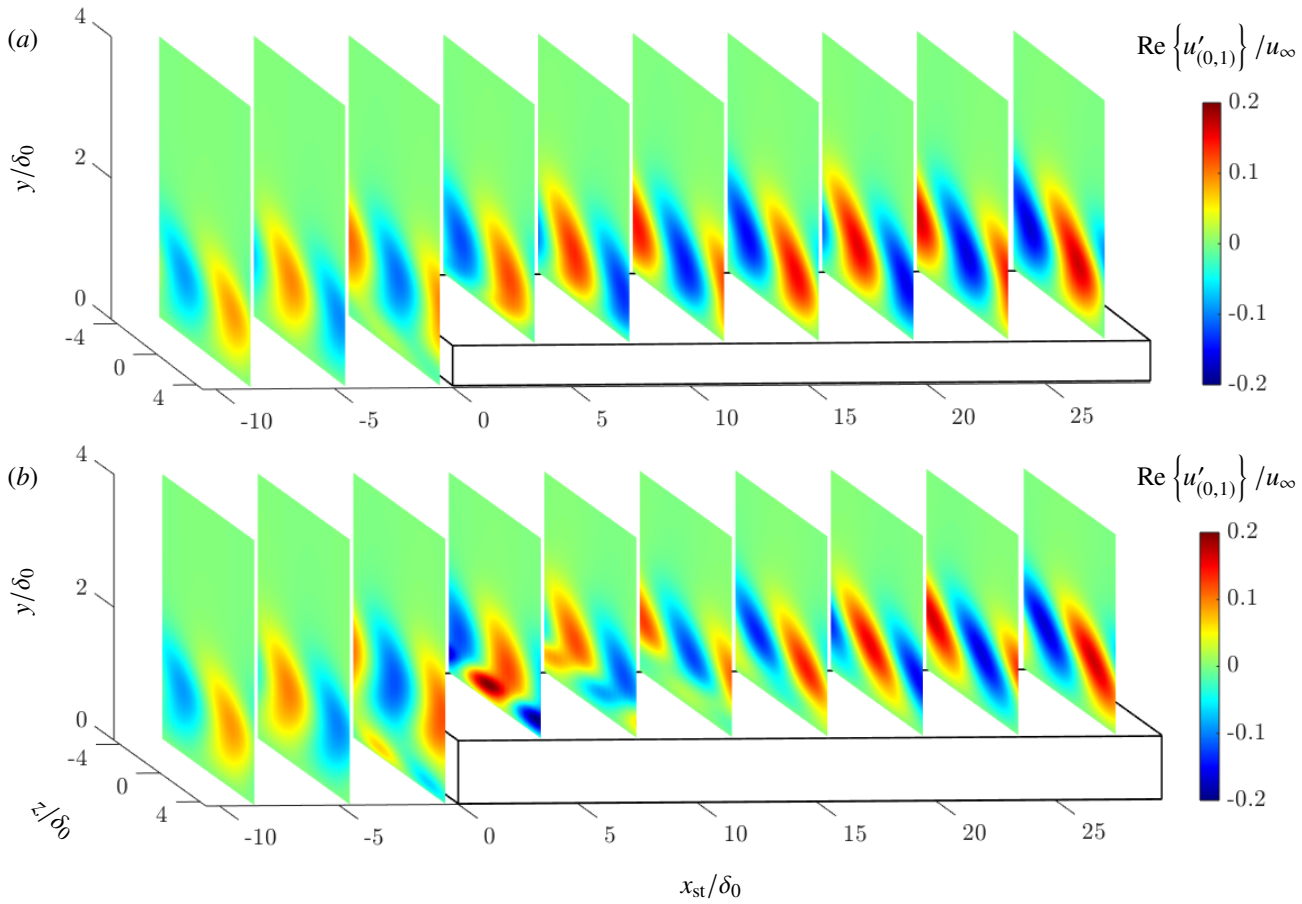

Figure 7 Three-dimensional organization of the streamwise-velocity-perturbation Fourier Mode $(0,1)$ **at the step location for step cases I (*a*) and III (*b*).**

underneath the core of the incoming instability and it undergoes a phase evolution in the x-direction different than that of the upper part of the pre-existing disturbance. In a fashion similar to the region upstream of the step, we identify a secondary near-wall peak in the perturbation shape downstream of the step, which is in linked to the near-wall streaks. We capture manifestations of this secondary lobe in the shape function for all $x_{st} > 0$ in the near-step region and for all step configurations.

The system of streaks in the upstream and the downstream vicinity of the step displays a different relative organization when considering the streamwise and the spanwise velocity components. In step case III, upon comparison between the core amplitude values of the incoming crossflow instability and the near-wall streaks, we find significant differences downstream of the step in the case of $u'_{(0,1)}$ (Fig. 7 (*b*)). Contrarily, in the case of $w'_{(0,1)}$, the cores of the original instability and the near-wall streaks are hard to visually differentiate downstream of the step, see Fig. 22 (*b*) in the Appendix. Upstream of the step, the trend is reverted. In the case of $w'_{(0,1)}$, the amplitude ratio between the core of the mode shape and the near-wall lobe is closer to one than in the case of $u'_{(0,1)}$. This is illustrated in Fig. 7 (*b*) and Fig. 22 (*b*) in the Appendix, but appears more evident in Fig. 8 and Fig. 23 in the Appendix.

Interestingly, we find that downstream of the step, the streamwise position of maximum amplitude of the near-wall lobe is not at the exact step corner, but at a small finite distance from it, see Fig. 8 and Fig. 23 in the Appendix. Initially close to the step corner, the secondary peak is weak in step case II, and very weak in step case I. In step case III, the near-wall lobe attains significantly larger amplitude values than the primary peak. For increasing x, the secondary lobe in step cases I and II rapidly merges back to the main profile, whereas in step case III, it undergoes strong decay in amplitude and, eventually, it becomes a local minima rather than a local maxima. This is highlighted in Fig. 9 depicting the evolution of the shape function in the streamwise direction downstream of the step. Further downstream, the part of

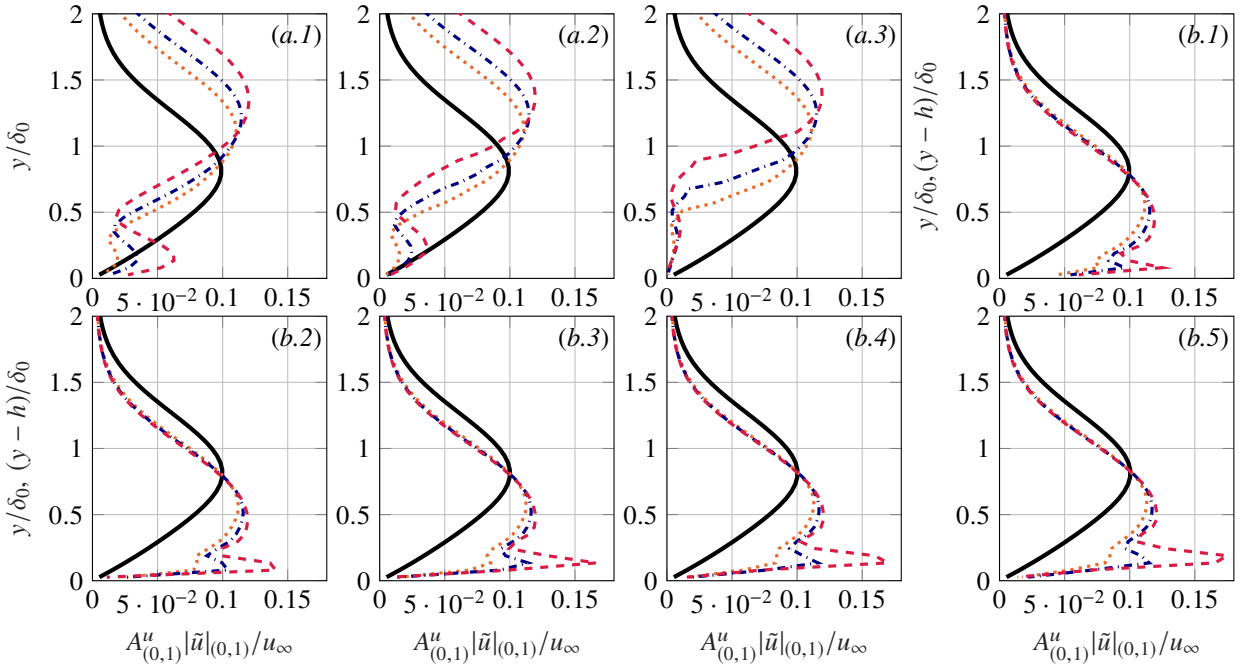

Figure 8 **Profiles of $A^u_{(0,1)}|\tilde{u}|_{(0,1)}$ at $x_{st}/\delta_0 = -0.32$ (*a.1*), -0.16 (*a.2*), -0.05 (*a.3*), 0.11 (*b.1*), 0.22 (*b.2*), 0.38 (*b.3*), 0.54 (*b.4*), 0.65 (*b.5*). Clean case (solid black), step case I (dotted orange), II (dash-dotted blue), III (dashed red).**

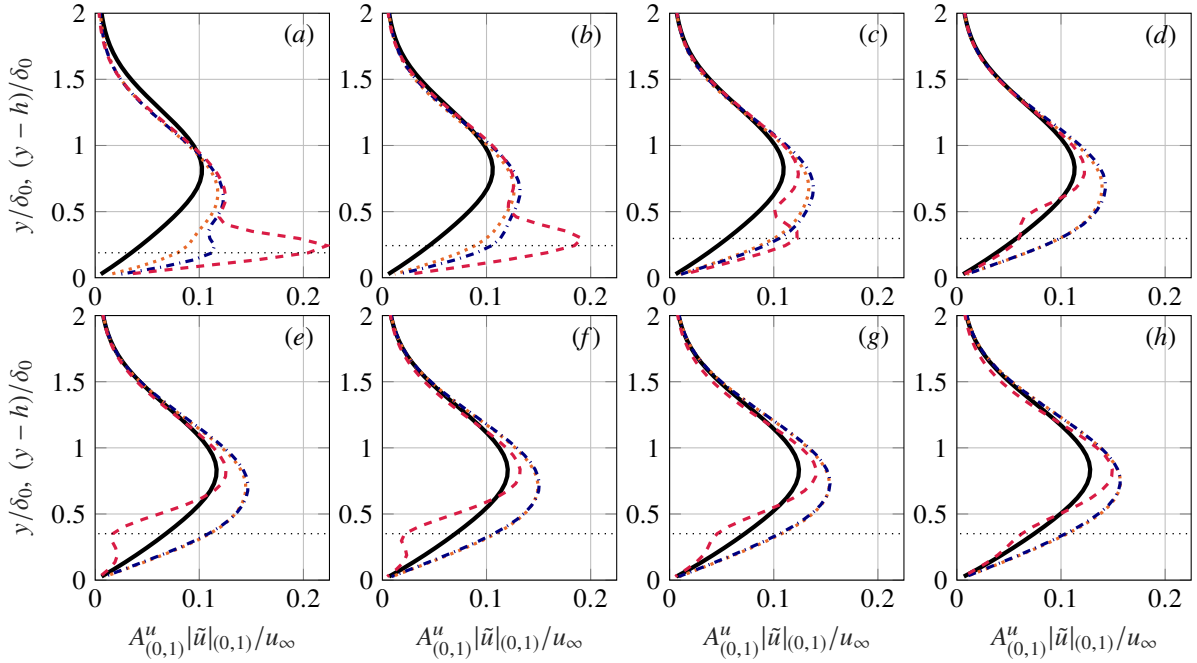

Figure 9 **Profiles of $A^u_{(0,1)}|\tilde{u}|_{(0,1)}$ at $x_{st}/\delta_0 = 2$ (*a*), 4.14 (*b*), 6.29 (*c*), 8.43 (*d*), 10.57 (*e*), 12.71 (*f*), 14.86 (*g*), 17 (*h*). Clean case (solid black), step case I (dotted orange), II (dash-dotted blue), III (dashed red). Wall-normal position of the secondary inflection point in step case III base flow.**

the profile associated to the near-wall indentation gradually relaxes back towards a configuration closer to that displayed by the no-step perturbation profile (Fig. 9 (*h*)). The existence of a secondary lobe in the shape function downstream of the step has been reported previously, see for instance Tufts et al. [2], Cooke et al. [10], or Eppink [23]. In particular, we find very good qualitative agreement between the results of Fig. 9 and the results presented by Tufts et al. [2] at the downstream vicinity of the step.

Sufficiently downstream of the step, the overall shape of Fourier mode $(0,1)$ in Fig. 7 (*b*) and Fig. 22 (*b*) in the Appendix gradually becomes elongated and tilts anti-clockwise. This shape transformation is observed to occur in parallel to the process by which the near-wall streaks become weaker and eventually disappear in x.

D. Correlation with base-flow features

We next refocus the attention to main elements of the base flow. Figure 10 (*c*,*d*) reproduces the results of Fig. 7 at the centerplane, i.e., at $z = 0$. To aid in the identification of base flow mechanisms with potential to trigger perturbation growth, we superimpose relevant features of the base flow on Fig. 10, namely, the location of $u_b = 0$, $w_{s,b} = 0$, $d^2u_b/dy^2 = 0$, and $d^2w_{s,b}/dy^2 = 0$. Additionally, Figure 10 (*a*,*b*) portrays the evolution of the total perturbation system.

Solid black lines in Fig. 10 are the loci of inflection points in the crossflow component. Upon comparison with the

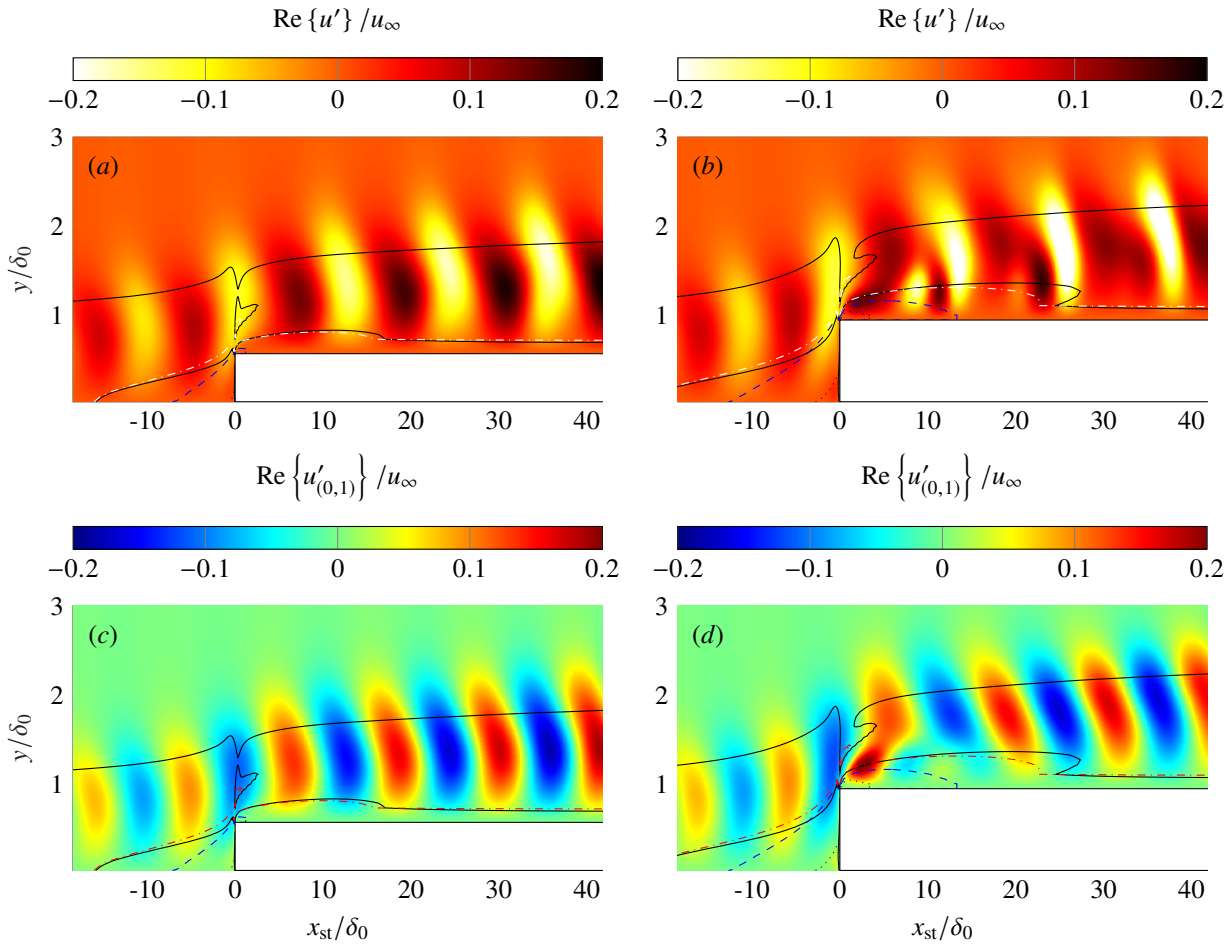

Figure 10 Streamwise-velocity-perturbation structure at the step, represented at the centreplane ($z = 0$)**: total perturbation field (*a*,*b*), perturbation Fourier mode** $(0,1)$ **(*c*,*d*) for step case I (*a*,*c*) and step case III (*b*,*d*). Loci of points of base flow features:** $d^2w_{s,b}/dy^2 = 0$ **(solid line),** $d^2u_b/dy^2 = 0$ **(dash-dotted line),** $w_{s,b} = 0$ **(dashed line),** $u_b = 0$ **(dotted line).**

results of the no-step case, the upper solid black line in Fig. 10 is associated to the inflection point in the crossflow component which originally gives rise to the crossflow instability. It undergoes a distortion in spatial organization at the step which increases with the height of the step. However, a major difference between the smooth and the step cases is the appearance of a prominent second family of inflection points in the crossflow component. They arise near the wall and close to the step, both upstream and downstream of it, see Fig. 10. Additionally, Fig. 9 depicts the wall-normal location of this secondary step-induced inflection point relative to the wall-normal distribution of the perturbation shape function. Hosseinverdi and Fasel [14] study instability mechanisms of swept laminar separation bubbles. They report the existence of a secondary inflection point in the crossflow component as well. Similar to the step cases of this work, it emerges in a region of adverse pressure gradient and they associate it to reversal of the crossflow component [14].

In the largest step case, we observe correlation between the location of this second family of inflection points downstream of the step and the core of the secondary near-wall peak in the mode shape of $u'_{(0,1)}$ (Fig. 9). Correlation is reasonably good but deteriorates when the near-wall lobe is measured in the spanwise-velocity component. A family of step-induced inflection points in the base flow streamwise-velocity component, u_b, is capture as well. Its spatial organization resembles that of the second family of inflection points in the crossflow component, see dash-dotted lines in Fig. 10. Upon performing a local linear Orr-Sommerfeld analysis on the base flow upstream and downstream of the step considering $\beta = \beta_0$, we do not identify additional unstable eigensolutions which are not present in the clean case, and which could potentially be associated to a new inviscid instability mechanism arising at the step. Nonetheless, this is not conclusive given the strong assumptions inherent to the Orr-Sommerfeld approach [15].

Tufts et al. [2] argue that the secondary peak in the shape function profile develops as a result of the interaction between the incoming instability and the downstream region of flow recirculation. There is little evidence in our DNS to support such claim. We capture manifestations of the near-wall peak for all $x_{\mathrm{st}} > 0$ in the near-step regime. Nonetheless, flow reversal in the basic flow starts at a slightly more downstream position, at $x_{\mathrm{st}}/\delta_0 = 0.22$ and 0.16 in step cases II and III respectively (Table 2). Furthermore, manifestations of the secondary lobe are measured for all step heights, whereas in step case I we do not capture flow reversal downstream of the step. Cooke et al. [10] report two peaks in their shape function profile as well, despite not capturing downstream flow separation in any of their step configurations. Tufts et al. [2] support their argumentation by finding that the secondary peak is at the same wall-normal position than the downstream area of flow recirculation. In a similar fashion, Eppink and Casper [8] indicate good agreement between the location of the near-wall peak in the perturbation shape and the region of flow separation. However, this is not the case in our results. Upon visual inspection, we find that the core of the near-wall lobe in the streamwise-velocity-perturbation Fourier mode $(0,1)$ is located above the region featuring $u_b < 0$ in the base flow. We remark that the same conclusion is drawn when reversal in the streamwise-velocity component is characterized using the spanwise-average developed flow solution instead, or when the perturbation shape accounts for the addition of the primary disturbance and its associated sub-harmonics.

E. Stationary secondary perturbations

In section IV, we quantitatively characterize the amplitude evolution of the incoming instability upon interaction with the step. However, before attributing a stabilizing or destabilizing effect of the step, it is paramount to clarify to what degree the near-wall system of streaks described above can be assumed to be a structure distinct to the pre-existing instability. To aid in the identification of coherent perturbation structures, we compute the Q-criterion [24] of the perturbation field $(0,1)$. We evaluate the Q-criterion in the following manner:

$$Q'_{(0,1)} = \frac{1}{2}\left(||\mathbf{R}'_{(0,1)}|| - ||\mathbf{S}'_{(0,1)}||\right), \tag{10}$$

where

$$\begin{aligned} ||\mathbf{R}'_{(0,1)}|| &= \frac{1}{2}\left\{\left(\omega'_{x,(0,1)}\right)^2 + \left(\omega'_{y,(0,1)}\right)^2 + \left(\omega'_{z,(0,1)}\right)^2\right\}, \\ ||\mathbf{S}'_{(0,1)}|| &= \sum_{i,k=1}^{i,k=3}\left\{\frac{1}{2}\left(\frac{\partial m'_i}{\partial x_k} + \frac{\partial m'_k}{\partial x_i}\right)\right\}^2, \end{aligned} \tag{11}$$

and $m'_1 = u'_{(0,1)}$, $m'_2 = v'_{(0,1)}$, $m'_3 = w'_{(0,1)}$, $x_1 = x$, $x_2 = y$, $x_3 = z$, real part implied.

Definition 10 is applied to the perturbation field $(0,1)$ solely, i.e., without the addition of the base flow and the sub-harmonic components, since the current aim lies in the identification of vortical structures developing in the

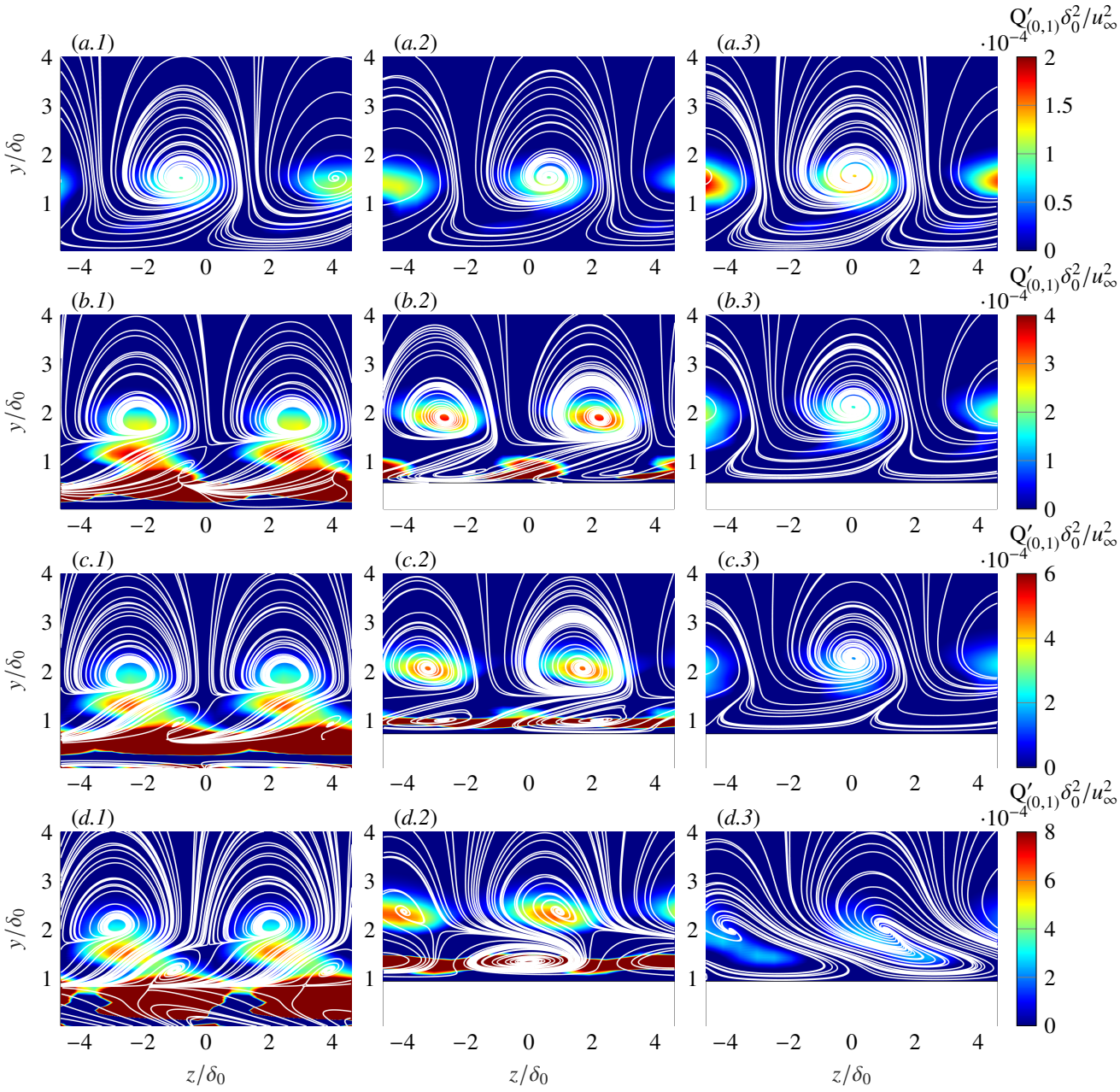

Figure 11 Q-criterion of perturbation field $(0,1)$ **at** y-z **planes with integrated streaklines of the inviscid-streamline-oriented velocity perturbation field** $(0,1)$**. Planes located at the upstream vicinity of the step** (1)**, at the downstream vicinity of the step** (2)**, at a constant position further downstream** (3)**. Clean case:** $x_{\mathrm{st}} = -1\delta_0$ **(*a.1*),** $3\delta_0$ **(*a.2*),** $15\delta_0$ **(*a.3*); step case I:** $x_{\mathrm{st}} = -0.7h$ **(*b.1*),** $1.5h$ **(*b.2*),** $15\delta_0$ **(*b.3*); step case II:** $x_{\mathrm{st}} = -0.7h$ **(*c.1*),** $2h$ **(*c.2*),** $15\delta_0$ **(*c.3*); step case III:** $x_{\mathrm{st}} = -0.7h$ **(*d.1*),** $3h$ **(*d.2*),** $15\delta_0$ **(*d.3*).**

fundamental perturbation space. Marxen et al. [25], for instance, study mechanisms of three-dimensional disturbances in a pressure-induced separating boundary layer. They identify disturbances in the form of streamwise perturbation vortices through visualization of isosurface of λ_2 [26] in the perturbation field. Under the definition of Eq. 10, we characterize regions of vortical motion in the perturbation organization as regions with excess of rotation rate relative to the strain rate, i.e., where $Q'_{(0,1)} > 0$.

Furthermore, in an attempt to shed light onto the nature and characteristics of the near-wall perturbation streaks, we consider the representation of the perturbation field expressed on the inviscid-streamline-aligned coordinate system. We evaluate the vorticity of the field defined in Eq. 7 in the direction x_s as

$$\omega'_{xs,(0,1)} = \frac{\partial w'_{s,(0,1)}}{\partial y_s} - \frac{\partial v'_{s,(0,1)}}{\partial z_s}, \tag{12}$$

with

$$\begin{aligned} \frac{\partial w'_{s,(0,1)}}{\partial y_s} &= \frac{\partial w'_{s,(0,1)}}{\partial y}, \\ \frac{\partial v'_{s,(0,1)}}{\partial z_s} &= \frac{\partial v'_{s,(0,1)}}{\partial z}\frac{\partial z}{\partial z_s} = \frac{\partial v'_{s,(0,1)}}{\partial z}\cos(\varphi), \end{aligned} \tag{13}$$

real part implied. Figure 11 displays y-z planes of $Q'_{(0,1)}$ with streaklines of the two-dimensional field defined by the inviscid-streamline-aligned perturbation components, $v'_{s,(0,1)}$ and $w'_{s,(0,1)}$, at the plane. We present results for the smooth and all step cases. Figure 11 (1) is representative of the immediate upstream vicinity of the step, Fig. 11 (2) is representative of the immediate downstream vicinity of the step, and Fig. 11 (3) shows a much downstream position, yet still in the near-step regime.

First, a representation of the primary crossflow disturbance when it develops over the smooth flat plate is shown in Fig. 11 (*a*). As expected, the instability manifests itself as spanwise-alternating counter-rotating vortices [14]. They are counter-rotating since the vorticity of the perturbation field $(0,1)$ in the x_s direction features opposite values (but equal in absolute value) at the core of the swirling motion in z-consecutive vortices. Furthermore, the core of the perturbation vortices matches well the location of *large* positive values of $Q'_{(0,1)}$.

When considering the smallest step case, far upstream of the step, the organization of the projected streaklines is identical to that of the no-step case. At the immediate upstream vicinity of the step, it suddenly displays a significantly different organization, featuring a three-layer structure in the wall-normal direction. First, the core and the upper part of the original perturbation vortices essentially maintain their topology. Second, there is a convoluted pattern of streaklines close to the wall. In between, we capture the onset of a new family of weak coherent perturbation vortices distributed in the spanwise direction and with the same spanwise wavenumber than the pre-existing vortices. Figure 11 (*b.1*) is representative of this. Therefore, Fourier mode $(0,1)$ contains at least two main distinct vortical structures within: the perturbation vortices associated to the pre-existing crossflow instability and secondary vortices which arise immediately upstream of the step. At the streamwise position of inception of the latter, $\omega'_{xs,(0,1)}$ displays clear patches which visually match the location of the secondary vortices. Consecutive spanwise patches feature opposite values of vorticity, thus the new vortices counter-rotate with respect to each other as well. Furthermore, we identify isolated patches of *large* $Q'_{(0,1)}$ very close to the wall, which could point towards the existence of an additional perturbation structure.

Just after passing the step corner, the secondary vortices undergo distortion in shape. They rapidly re-organize in x and remain underneath of the primary vortices and close to the wall. When moving further downstream, the secondary vortices eventually disappear and the overall streakline organization becomes visually similar to that of the smooth case, see Fig. 11 (*b.3*). In step case II, we observe an evolution of the perturbation vortex system rather similar to that of step case I, see Fig. 11 (*c*). However, a main difference is the increased strength of the secondary vortices downstream of the step corner. This is consistent with the fact that the near-wall lobe in the perturbation shape increases its strength when the step height is increased. Furthermore, the secondary vortices are generally elongated in the spanwise direction, which is a distinctive attribute of the near-wall system of streaks illustrated in Fig. 7 and Fig. 22 in the Appendix. In essence, the secondary perturbation vortices, the near-wall streaks, and the secondary peak in the perturbation shape function downstream of the step are manifestations of a common mechanism.

In step case III we capture strong differences in the vortical activity around the step when compared to the smaller step cases. Figure 12 complements Fig. 11 and portrays the evolution of the perturbation vortices at additional intermediate y-z planes for step case III solely. Upstream of the step, secondary vortices are easier to visually identify. Downstream of the step, the near-wall vortices undergo very strong growth and distortion in shape. At $x_{st}/\delta_0 = 1.9$, the secondary vortices are significantly more comparable in size to the primary vortices than in step cases I and II; the region of influence of the secondary vortices extends approximately up to $1h$ above the wall, see Fig. 12 (*a*). At approximately $x_{st}/\delta_0 = 2.5$ (Fig. 12 (*b*) and Fig. 11 (*d.2*)) the secondary vortices display elongation in the spanwise direction. At this streamwise station, they become much stronger than the original perturbation vortices; the field $\omega'_{xs,(0,1)}$ features significantly larger (absolute) values in the region of influence of the secondary vortices as compared to that of the

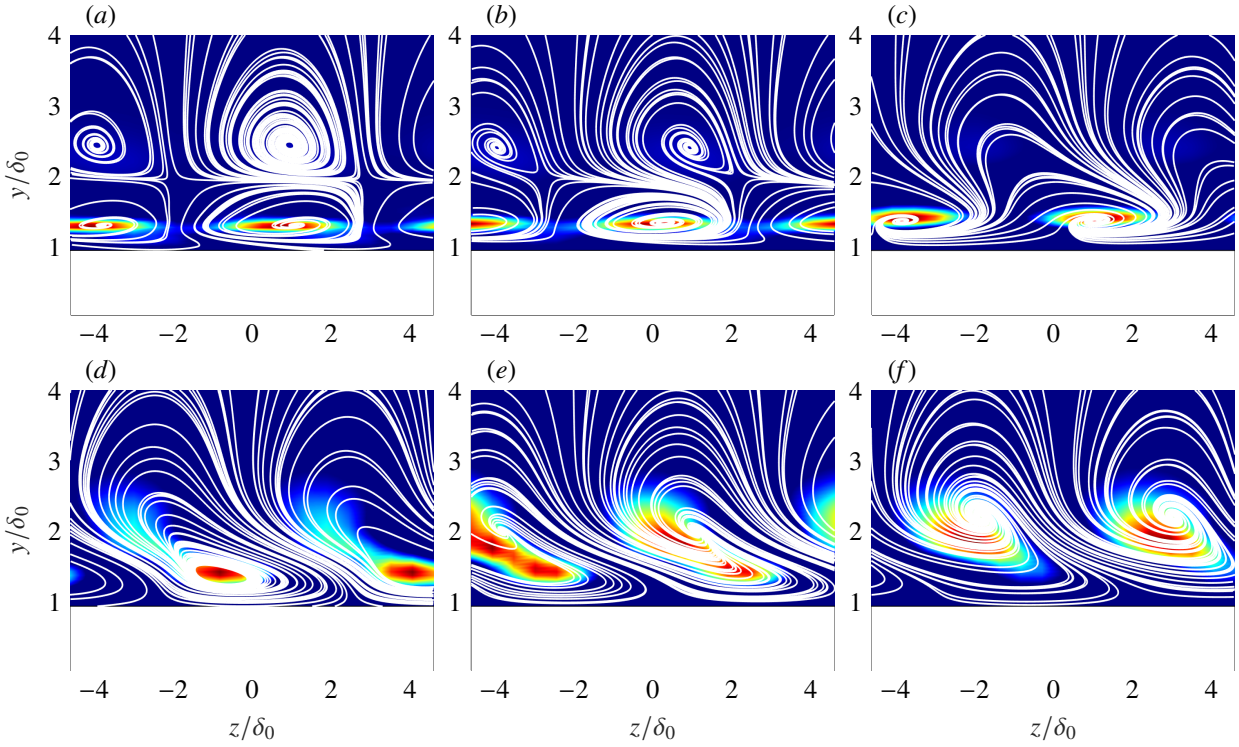

Figure 12 Q-criterion of perturbation field $(0,1)$ **at** y-z **planes with integrated streaklines of the inviscid-streamline-oriented velocity perturbation field** $(0,1)$ **of step case III. Planes located at** $x_{\mathrm{st}}/\delta_0 = 1.9$ **(*a*),** 2.5 **(*b*),** 6 **(*c*),** 13 **(*d*),** 15 **(*e*),** 18 **(*f*). Color expresses maximum in-plane values, relative to each plane.**

primary vortices. We note that the secondary vortices downstream of the step require a small finite streamwise distance to feature their maximum strength. In a similar fashion, the near-wall lobe in the perturbation shape function does not develop its peak amplitude at $x_{\mathrm{st}} = 0$ identically, but slightly downstream of it (Fig. 8). When moving further downstream from the step corner, the near-wall vortices in step case III evolve in a fashion similar to the near-wall system of streaks depicted in Fig. 7 and Fig. 22 in the Appendix: their strength rapidly decreases in x, and their cores follow a three-dimensional trajectory different than that of the pre-existing structures.

Initially near the step corner, a primary vortex counter-rotates with respect to the secondary structure located approximately underneath. Figure 11 (*b.2*), (*c.2*), and (*d.2*) portrays a streamwise station which is representative of this. When moving downstream, the phase difference between the lower and the upper part of Fourier mode $(0,1)$ changes significantly. This is illustrated in Fig. 13 portraying $\phi^u_{(0,1)}$ at the vicinity of the step. As a consequence, sufficiently downstream, the secondary vortices have become closer to an equivalent co-rotating primary vortex structure above and we observe gradual vortex merging between primary and secondary perturbation vortices. In Figs. 11 (*d.3*) and 12 (*d*), the organization of the perturbation streaklines shows a unique primary entity with a main swirling motion; the original patches of *large* $Q'_{(0,1)}$ close to the wall and far from the wall start to merge. The spatial organization of the primary and secondary vortices at the beginning of the merging process causes the resulting entity to initially feature an elongated shape (Figs. 11 (*d.3*) and 12 (*e*)), which is seemingly tilted anti-clockwise with respect to the remaining primary structure in the clean and smaller step cases (Figs. 11 (*a.3*), (*b.3*), and (*c.3*)). This is associated to the characteristic elongated shape that Fourier mode $(0,1)$ eventually exhibits downstream of the step, as previously pointed out and illustrated in Fig. 7 (*b*), and Fig. 22 (*b*) in the Appendix.

The existence of secondary vortical structures developing underneath of the pre-existing ones at the step was reported by Eppink [27]. In her results, the manifestation of these vortices is presented in the total flow field. In the model proposed by Eppink [27], secondary vortices captured immediately upstream and downstream of the step are distinct structures. The secondary vortices induced upstream generate a perturbation in the wall-normal direction. This perturbation is maintained downstream of the step close to the wall, at the location of the second step-induced inflection

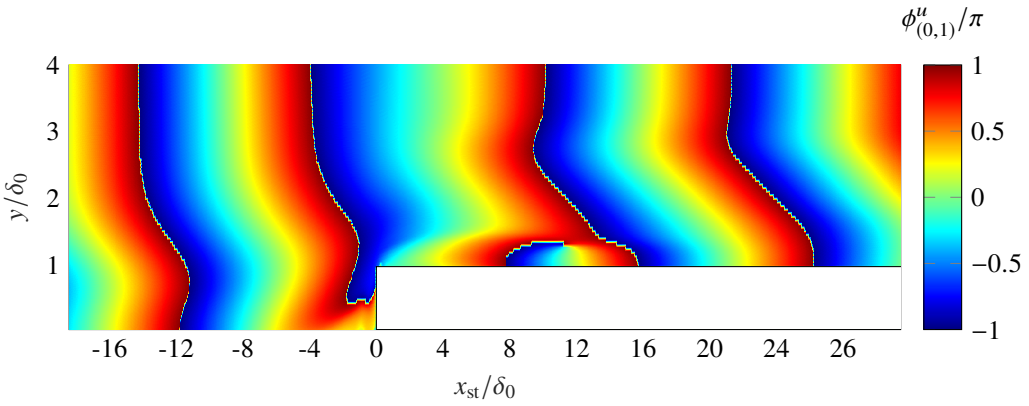

Figure 13 Phase of the streamwise-velocity-perturbation Fourier mode $(0,1)$ **around the step of case III.**

point in the crossflow component. A new secondary near-wall vortex can develop due to the strong crossflow component *right at the step*, enhanced by the sustained wall-normal perturbation generated upstream [27]. The convoluted organization of the perturbation field at the step makes it hard for us to interpret whether two distinct secondary vortices emerge immediately upstream and downstream of the step or, on the contrary, a single structure persists and undergoes shape distortion while passing very close to the step corner. In step case III, immediately upstream of the step, at $x_{st}/\delta_0 = -0.53$, we capture the core of the secondary vortices at $y/\delta_0 = 1.17$. Immediately downstream of the step, at $x_{st}/\delta_0 = 0.59$, the core of the secondary vortices is measured at $y/\delta_0 = 1.17$ as well. This correlation is not conclusive, but it suggests that the secondary vortices captured downstream of the step are a single structure induced upstream of it. Moreover, we remark that, in step case III, the wall-normal location of the second near-wall inflection point in the base flow crossflow component lies at $y/\delta_0 = 0.95$ for $x_{st}/\delta_0 = -0.53$ and at $y/\delta_0 = 1.11$ for $x_{st}/\delta_0 = 0.59$.

On the one hand, Eppink [23, 27] postulates that the destabilizing effect of the step-induced inflection points –which cause the velocity profiles to be of inviscidly unstable nature– is mainly responsible for the strong perturbation growth downstream of the step. On the other hand, near-wall vortices with an organization which resembles the one presented in this work have been identified in other studies concerning two-dimensional steps [28, 29] and linked to transient growth mechanisms. Within the context of these investigations, an incoming pre-existing boundary layer instability was not imposed, thus similarities ought to be addressed cautiously. Breuer and Kuraishi [30] studied transient growth effects in a three-dimensional boundary layer. They pointed out that in boundary layers featuring large crossflow, transient growth can boost the growth of crossflow vortices, which afterwards follow the Orr-Sommerfeld type of mechanism. The appearance of streak-like regions can be a manifestation of this [30].

F. Evolution of the sub-harmonic content at the step

Until now, we have put the focus on main structures which belong to the fundamental perturbation space. Nonetheless, the sub-harmonic instability waves are known to play a relevant role in the interaction between the incoming disturbance and the step, see Eppink [23] for instance. Therefore, in this section we center the attention to the behaviour of Fourier modes $(0,2)$-$(0,4)$.

As mentioned in previous sections, for the choice of initial amplitude of the crossflow mode imposed at the inflow, low activity of the sub-harmonic content is triggered at $x_{st} = 0$ in the smooth case (section III.A). However, when considering the step cases, significant activity of the sub-harmonic components is captured at the step. Figures 14 and 15 portray $A^u_{(0,j)}|\tilde{u}|_{(0,j)}, j = 2,3,4$ in step cases I and III, respectively. Additionally, Figs. 14 and 15 superimpose the loci of points of $d^2w_{s,b}/dy^2 = 0$ in the base flow. Upstream of the step, the shape function of Fourier mode $(0,2)$ displays a double-peak structure which resembles the one observed in the smooth case, see section III.A. This topological feature is common in all step configurations. However, this is hard to visualize in Figs. 14 and 15 due to the sub-harmonic growth downstream of the step, which hinders a more comprehensive global representation.

At the step corner in the smallest step case, $A^u_{(0,j)}|\tilde{u}|_{(0,j)}, j = 2,3,4$ increases suddenly in x in the region where the secondary peak in the shape function of Fourier mode $(0,1)$ in step case III is prominent. See for instance, Fig. 14 (*b*,*c*,*d*) compared to Fig. 15 (*a*). For increasing x, this region of enhanced sub-harmonic growth at the step corner and

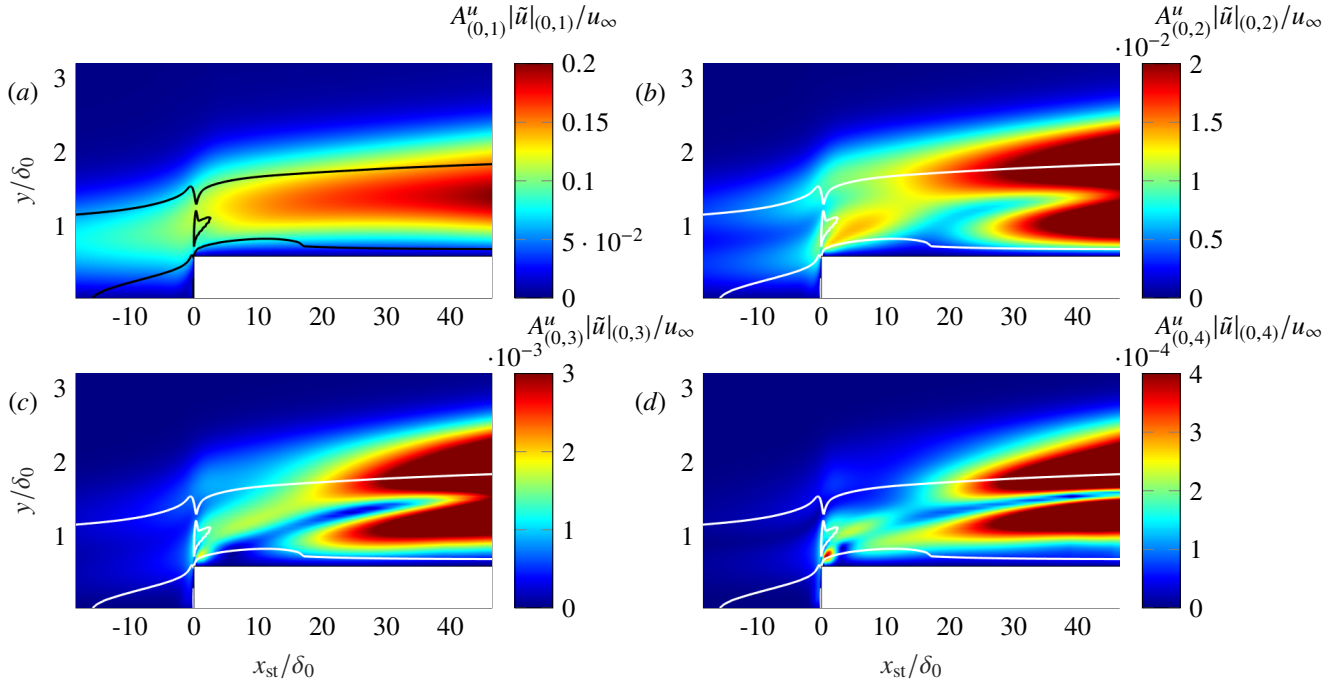

Figure 14 Shape function of Fourier mode $(0,1)$ **(*a*),** $(0,2)$ **(*b*),** $(0,3)$ **(*c*),** $(0,4)$ **(*d*) in step case I. Solid black and white lines are the loci of points in the base flow with** $d^2w_{s,b}/dy^2 = 0$**.**

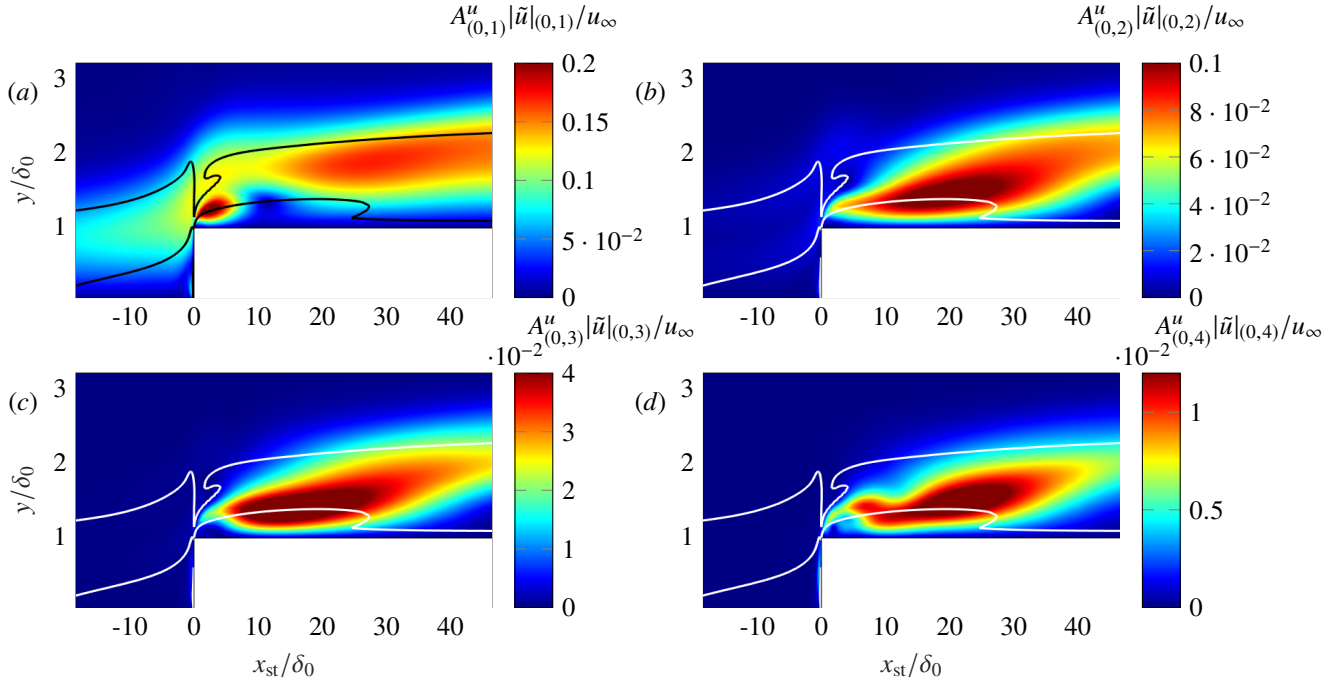

Figure 15 Shape function of Fourier mode $(0,1)$ **(*a*),** $(0,2)$ **(*b*),** $(0,3)$ **(*c*),** $(0,4)$ **(*d*) in step case III. Solid black and white lines are the loci of points in the base flow with** $d^2w_{s,b}/dy^2 = 0$**.**

the upper lobe of the incoming perturbation structure tend to connect in space. Sufficiently downstream of $x_{st} = 0$, all sub-harmonic mode shapes manifest a (distorted) double-peak structure again.

In step case III, we capture sudden sub-harmonic amplification at $x_{st} = 0$ as well, in a fashion similar to the behaviour display by Fourier mode $(0, 1)$. In the largest step, the secondary peak in the perturbation shape of the fundamental Fourier mode decays rapidly in x, see section III.C; however, this is not the case when considering Fourier modes $(0, 2)$-$(0, 4)$. When moving downstream of the step corner, the sub-harmonic disturbance growth initiated at $x_{st} = 0$ persist close to the wall and amplifies. We find strong correlation between the spatial location of peak amplitude in the shape of Fourier modes $(0, 2)$-$(0, 4)$ and the location of the secondary inflection points in the base flow downstream of the step. When moving further in x, the near-wall region of enhanced sub-harmonic activity gradually shifts upward, close to the location of the primary peak of the incoming fundamental disturbance.

The similarities between the behaviour of the fundamental and the sub-harmonic Fourier modes at $x_{st} = 0$ suggests the existence of a common mechanism responsible for the sudden disturbance growth close to the wall. A main question that arises is whether, as discussed for mode $(0, 1)$, for the sub-harmonic instabilities this is similarly attributed to the effect of upstream secondary inflections points as suggested by Eppink [27] or due to transient growth mechanisms. By analogy, there exists the possibility that secondary stationary perturbations with spanwise wavenumbers of $\beta = j\beta_0$, j = 2,3,4... arise at the step corner as well. However, a major difference between the evolution of disturbances with $\beta = \beta_0$ and $\beta > \beta_0$ further downstream of $x_{st} = 0$ is the apparent insensitivity of the former to the secondary near-wall inflection points. Thus, the evolution of Fourier modes $(0, 2)$-$(0, 4)$ in the large step case is in qualitative agreement with the model proposed by Eppink [27], which is partially not the case for Fourier mode $(0, 1)$. A possible explanation which ought to be further explored is the fact that high-order instability waves may be prone to amplification due to an Orr-Sommerfeld type of mechanisms when considering the distortion of the base flow induced by the step near the wall.

IV. Quantification of the impact of the step on the incoming stationary crossflow disturbance

A. Primary crossflow instability

We next refocus the attention to a main objective of this investigation, which is to quantitatively asses the effect of the step on the stability properties of the fundamental crossflow disturbance upon interaction. Figure 16 portrays the streamwise evolution of $A^u_{(0,1)}$, the amplitude of the streamwise-velocity-perturbation Fourier mode $(0, 1)$. Immediately upstream of the step, $A^u_{(0,1)}$ grows gradually for all step configurations. Downstream of the step, the amplification of

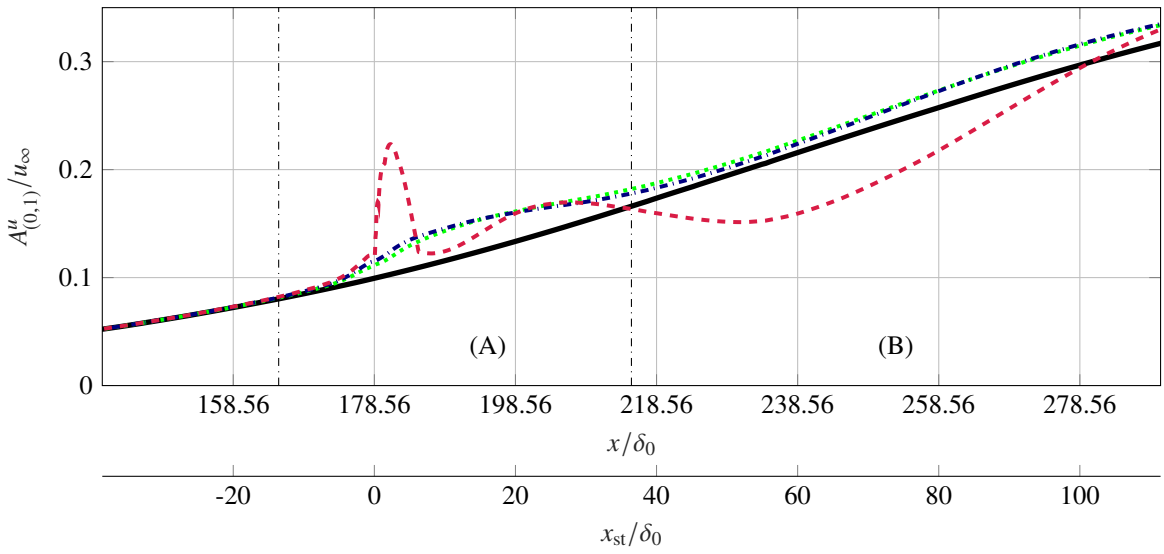

Figure 16 Streamwise evolution of the amplitude of the streamwise-velocity-perturbation Fourier mode $(0, 1)$ **for the clean case (solid black), step case I (dotted green), II (dash-dotted blue), III (dashed red). Limits of zones (A,B) (dash-dotted black).**

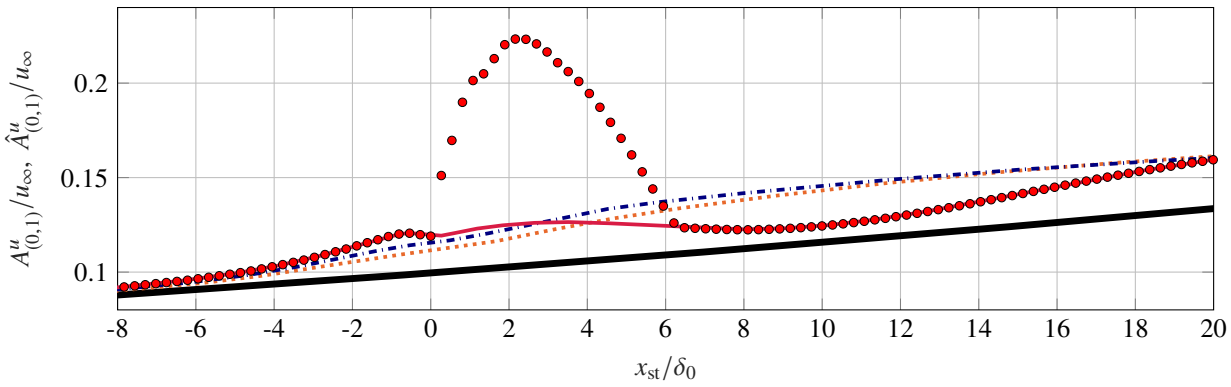

Figure 17 Streamwise evolution of the amplitude of Fourier mode $(0,1)$, $A^u_{(0,1)}$, in the clean case (thick solid black line), step case I (dotted orange line), II (dash-dotted blue line), III (red circles). Streamwise evolution of $\hat{A}^u_{(0,1)}$ in step case III (thin solid red line).

Fourier mode $(0,1)$ is gradual and extends over a *large* streamwise range for step cases I and II, see the zone denoted by "A" in Fig. 16. On the other hand, the trend followed by the curve of step III is characterized by a strong and sudden initial growth immediately downstream of the step followed by an abrupt strong decay. Further downstream, still within zone A, we observe a phase of mild amplification followed by a second phase of decay, which causes the curve of case III to eventually intersect the curve associated to the smooth configuration. We find the amplitude evolution of step case III near the step to be in very close qualitative agreement with PIV results presented by Eppink and Casper [8] (Fig. 9). In zone "B", the clean configuration generally features larger amplitude of the primary mode, when compared to the largest step; thus, sufficiently downstream, the incoming stationary instability is eventually stabilized with respect to the no-step case.

We next restrict the analysis to zone A in Fig. 16 encompassing the mechanisms of interaction in the near-step regime. As stated above, the curve of step case III undergoes a significantly different evolution than that of the curves associated to the smooth and smaller step cases. This is ascribed to the differences pointed out previously in the development of the perturbation structures at the step. In particular, we associate the sudden explosive growth of the curve of step III in Fig. 16 to the strong amplification in x of the near-wall lobe in the perturbation shape function. Figure 9 illustrates that the strength of the near-wall lobe eventually exceeds that of the primary peak. The amplitude of Fourier mode $(0,1)$, as formally defined in Eq. 4, is evaluated at the global maxima of the shape function in y. Consequently, at a small finite distance downstream of $x_{st} = 0$, the characterization of $A^u_{(0,1)}$ jumps discontinuously in the wall-normal direction from the original primary peak far from the wall to the secondary peak close to the wall. Further downstream, as the near-wall lobe undergoes strong amplitude decay in x, this trend is reverted.

In previous sections, we have established that the secondary lobe in the shape function profile, the system of near-wall streaks, and the secondary vortices are manifestations of a common perturbation mechanism arising close to the step, whereas the primary peak is associated to the core of the pre-existing instability. Thus, we believe that the classic approach used in other investigations –which relies on characterizing the amplification or stabilization of the incoming disturbance at the step by measuring the peak amplitude of the full perturbation shape– may lead to misleading interpretations. Upon using the global maxima of the perturbation profile for characterizing amplification of the pre-existing instability, close to the step for *large* steps, the growth of a secondary perturbation structure distinct to the main one is inherently measured. Or, at least, the growth of a perturbation structure which originally was part of the main one and, near the step, it decouples from it, undergoes a significantly different organization, and eventually disappears or merges with the core of the pre-existing one.

We propose that a more representative characterization of the effect of the step on the original disturbance is obtained when the amplitude of the perturbation shape function is measured at the wall-normal location of the original primary peak, continuously in x. Hereafter, this amplitude definition is denoted by $\hat{A}$, and $\hat{A}_{(0,1)} = \hat{A}_{(0,1)}(x)$. We observe that, for all x in the near-step regime, the streamwise-velocity-perturbation shape profile features at least one point with $d|\tilde{u}|_{(0,1)}/dy = 0$ and $d^2|\tilde{u}|_{(0,1)}/dy^2 < 0$ far from the wall, within the boundary layer region. Moreover, the wall-normal location of the primary peak changes smoothly in x as the perturbation system passes over the step. Figure 17 depicts

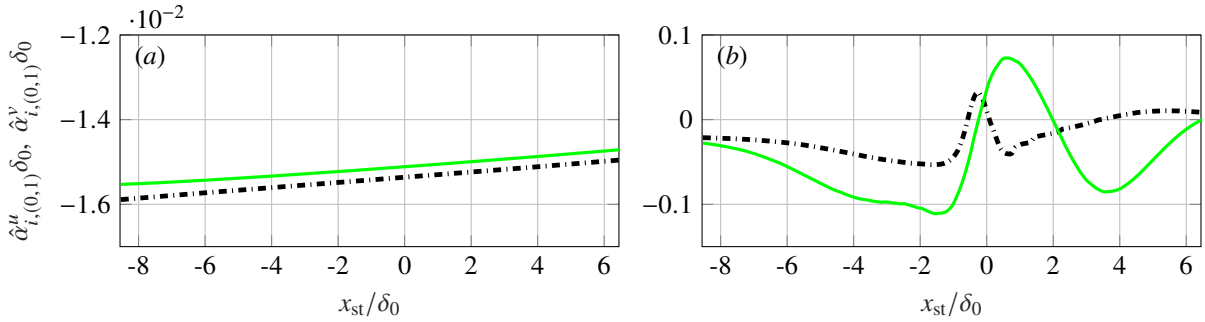

Figure 18 Growth rate of the streamwise- (dash-dotted black) and the wall-normal-velocity perturbation component (solid green) based on the definition of $\hat{A}_{(0,1)}$, in the clean case (*a*) and step case III (*b*).

the streamwise evolution of $A^u_{(0,1)}$ and $\hat{A}^u_{(0,1)}$ close to the step. In the smooth and step cases I and II, $A^u_{(0,1)} = \hat{A}^u_{(0,1)}$ since secondary peaks, if present, never surpass the primary ones in strength. However, in step case III we find very significant differences when comparing the streamwise evolution of $A^u_{(0,1)}$ and $\hat{A}^u_{(0,1)}$.

Moreover, when the aforementioned criterion for amplitude characterization is employed, we observe that different perturbation-velocity components display different growth rates around the step. We characterize the streamwise growth rate of the primary instability as

$$\hat{\alpha}^k_{i,(0,1)} = -\frac{1}{\hat{A}^k_{(0,1)}}\left(\frac{d\hat{A}^k_{(0,1)}}{dx}\right), \tag{14}$$

where k expresses the pertinent component of the state vector $\mathbf{q}$. Figure 18 portrays the streamwise evolution of $\hat{\alpha}^u_{i,(0,1)}$ and $\hat{\alpha}^v_{i,(0,1)}$ for the smooth (*a*) and step III (*b*) cases. In Fig. 18 (*a*), $\hat{\alpha}^u_{i,(0,1)} = \hat{\alpha}^v_{i,(0,1)}$ approximately. This behaviour is expected for a stationary crossflow instability developing in a quasi-parallel boundary layer. In Fig. 18 (*b*), however, the streamwise evolution of $\hat{\alpha}^u_{i,(0,1)}$ and $\hat{\alpha}^v_{i,(0,1)}$ is fundamentally different: immediately downstream of the step, $\hat{\alpha}^v_{i,(0,1)}$ attributes stabilization whereas $\hat{\alpha}^u_{i,(0,1)}$ attributes destabilization. This is contrary to observations performed by Eppink [27], who points out that the growth rates of the streamwise- and the wall-normal-perturbation components are *very similar* at the step. We presume that this observation refers to growth rate characterization based on peak amplitude evolution. Eppink [27] relates the similarity in the growth rate of different velocity components to the possibly linear nature of the disturbance mechanisms immediately downstream of the step. The discrepancy between the observations of Eppink [27] and the results presented above ought to be further explored in future work. Particularly, since our findings pose the question whether the crossflow instability interacting with the step can be fully described as a single eigenmode which amplifies all velocity components at a same rate in x.

To overcome the ambiguity in amplification characterization which arises from the particular choice of a state variable, it appears suitable to consider energy-based criteria. We introduce the following definition of disturbance kinetic energy:

$$\hat{E}_{(0,1)} = \frac{1}{2}\left\{\left(\hat{A}^u_{(0,1)}\right)^2 + \left(\hat{A}^v_{(0,1)}\right)^2 + \left(\hat{A}^w_{(0,1)}\right)^2\right\}, \tag{15}$$

which encompasses the evolution of the primary peak of all velocity-perturbation components simultaneously. We remark that $\hat{E}_{(0,1)} = \hat{E}_{(0,1)}(x)$. Definition 15 suffers from lack of consistency since $\hat{A}^u_{(0,1)}$, $\hat{A}^v_{(0,1)}$, and $\hat{A}^w_{(0,1)}$ are independently measured at different wall-normal positions. However, if the aim lies in quantifying the impact of the step on the incoming instability solely, characterizations based on the integration of the full perturbation profile may suffer from vagueness in the definition of the integration limits when segregating secondary perturbation effects.

The streamwise evolution of $\sqrt{2\hat{E}_{(0,1)}}$ is illustrated in Fig. 19. Upstream of the step, at approximately $x_{st}/\delta_0 = -16$, the curves of all step cases gradually deviate from the curve associated to the smooth case. At $x_{st} = 0$, the presence of the step has amplified the crossflow disturbance in all configurations. We observer that, the larger the step, the larger the amplification factor at $x_{st} = 0$. Downstream of $x_{st} = 0$, the curves of step cases I and II grow monotonically, at a rather

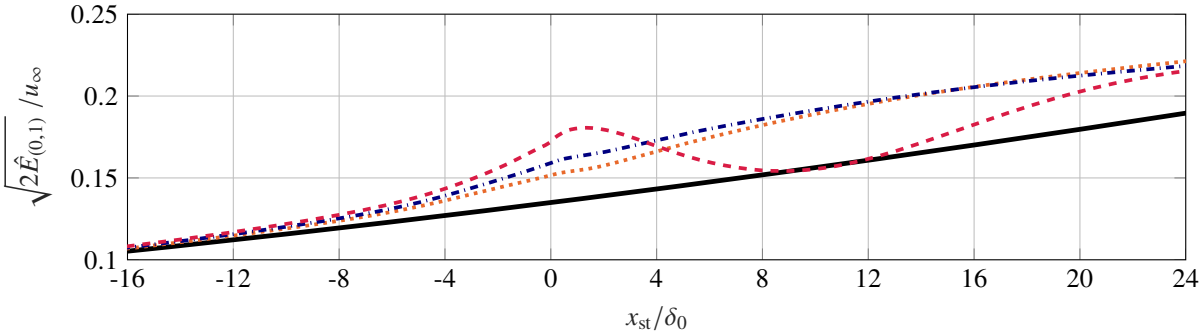

Figure 19 Streamwise evolution of $\hat{E}_{(0,1)}$ in the clean case (solid black), step case I (dotted orange), II (dash-dotted blue), III (dashed red).

constant rate. The curve of step case III, however, displays weak initial growth followed by an abrupt decay. The curve of step case III eventually intersect the curve associated to the smooth case before growing again. Therefore, for our largest step, the incoming primary crossflow disturbance undergoes strong stabilization slightly downstream of the step corner.

B. Total perturbation field

In section III.F, we have reported that significant activity of the sub-harmonic instability waves is triggered immediately downstream of $x_{st} = 0$ when considering our largest step. Thus, an accurate quantitative representation of the amplitude evolution of the total perturbation field at the step may require the addition of high-order Fourier modes to the methodology presented above. In this section, we extend the previous analysis by considering a Fourier representation of the perturbation field truncated at mode $(0, 3)$.

Upstream of the step, the second and the third sub-harmonic Fourier modes display amplitude values significantly smaller than that of the primary Fourier component. This is illustrated in Fig. 20 characterizing the streamwise evolution of $A^u_{(0,2)}$ and $A^u_{(0,3)}$ in step case I (a) and step case III (b), and is in line with results presented in section III.A. At the location of the step, $A^u_{(0,2)}$ and $A^u_{(0,3)}$ increase suddenly in x, a trend which may not necessarily be associated to amplification of the incoming perturbation structures. For different combinations of perturbation-velocity components, step heights, and Fourier components, the characterization of amplitude based on the global maxima of the shape function generally jumps discontinuously in the wall-normal direction at the location of the step in x. In a fashion

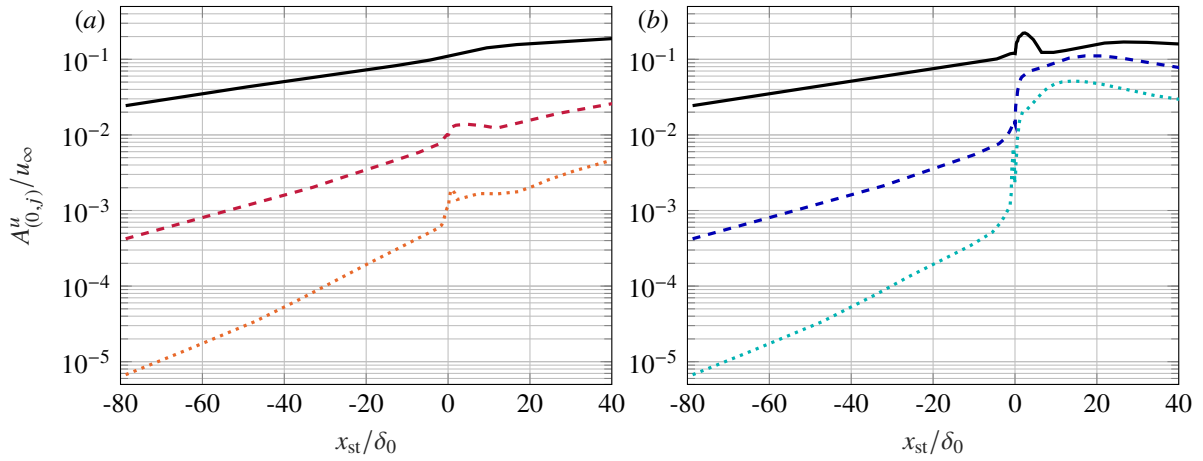

Figure 20 Streamwise evolution of the amplitude of the streamwise-velocity-perturbation Fourier mode $(0, 1)$ (solid), $(0, 2)$ (dashed), $(0, 3)$ (dotted) for step case I (a) and III (b).

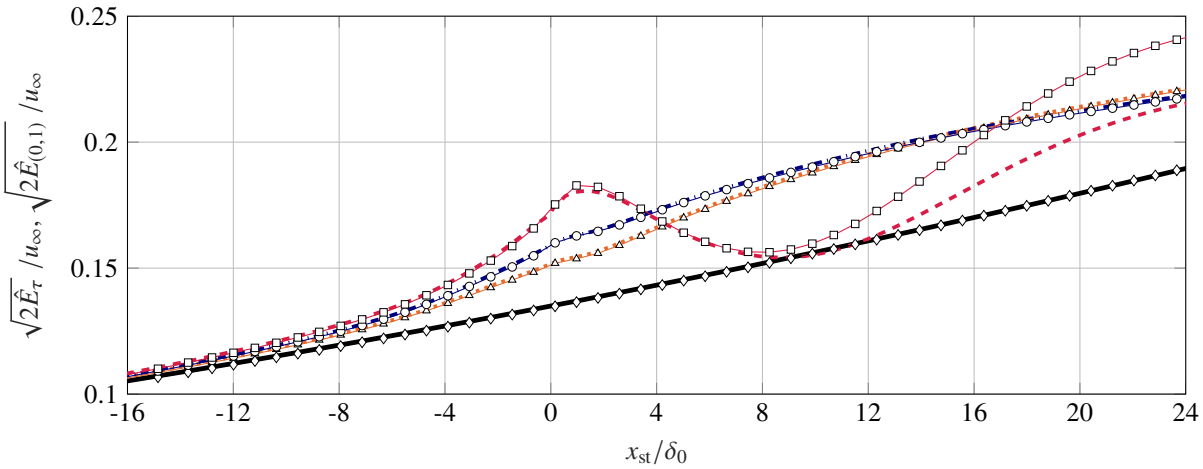

Figure 21 Streamwise evolution of $\hat{E}_{(0,1)}$: clean case (solid black), step case I (dotted orange), II (dash-dotted blue), III (dashed red). Streamwise evolution of $\hat{E}_\tau$: clean case (diamonds), step case I (triangles), II (circles), III (squares).

similar to the case of the fundamental Fourier mode, significant sub-harmonic disturbance growth close to the wall manifests as additional peak(s) in the perturbation shape of the high-order Fourier modes. New secondary peaks induced at the step corner may attain the largest amplitude value in y, *locally* downstream of $x_{st} = 0$.

The amplification of $A^u_{(0,2)}$ and $A^u_{(0,3)}$ at the location of the step is significantly stronger in step case III, when compared to step case I. Therefore, the mechanism which triggers disturbance growth at the step corner near the wall induces stronger amplification of the sub-harmonic content for increasing step heights. Similarly, the secondary lobe in the shape function of Fourier mode $(0,1)$ attains significantly larger amplitude values in step case III, as compared to step cases I and II (Fig. 9). Furthermore, in section III.F we have qualitatively described that, in step case III, the initial growth of sub-harmonic disturbance content at the step corner is sustained and amplified further downstream, close to the location of the secondary near-wall inflection point. Contrarily, when considering step case I, the near-wall effects downstream of the step are rather weak. Figure 20 quantitatively confirms this behaviour: in step case III, the strong growth of $A^u_{(0,2)}$ and $A^u_{(0,3)}$ at $x_{st} \approx 0$ is maintained and even enhanced immediately downstream, which is not the case for step configuration I.

With all, the sub-harmonic Fourier shape functions at the step exhibit an intricate topology. This poses the challenge of reproducing the methodology for amplitude characterization applied in the previous section identically. To track a main peak of the mode shape continuously in x when the pertinent sub-harmonic perturbation system passes over the step may be laborious for certain combinations of step heights and perturbation-velocity components. To overcome this predicament, we characterize amplitude evolution of the full perturbation field using the following definition of disturbance kinetic energy:

$$\hat{E}_\tau(x) = \frac{1}{2}\sum_{j=0}^{j=3}\sum_{k=1}^{k=3}\left\{A^k_{(0,j)}(x)\;|\tilde{q}^k|_{(0,j)}(x, s_{(0,1)}(x))\right\}^2. \tag{16}$$

In Eq. 16, j expresses a mode of the Fourier series, k expresses a velocity component of the state vector $\mathbf{q}$, and $s_{(0,1)}(x)$ is the wall-normal location of the primary peak of the streamwise-velocity-perturbation component of Fourier mode $(0,1)$, i.e., the wall-normal position associated to $\hat{A}^u_{(0,1)}$. In essence, Eq. 16 expresses a metric equivalent to Eq. 15; however, Eq. 16 considers Fourier modes $(0,0)$-$(0,3)$ and evaluates all velocity components at a common wall-normal position defined by the behaviour of the fundamental incoming instability.

Figure 21 reproduces the results of Fig. 19 and adds the characterization of Eq. 16 to compare the streamwise evolution of $\hat{E}_{(0,1)}$ and $\hat{E}_\tau$. As expected, $\hat{E}_\tau = \hat{E}_{(0,1)}$ in the smooth case near the virtual streamwise position of the step. When considering step cases I and II, the streamwise evolution of $\hat{E}_\tau$ and $\hat{E}_{(0,1)}$ are in close agreement. Hence, the sub-harmonic disturbance growth downstream of the step does not significantly impact the amplitude evolution of the full perturbation field at the wall-normal location of the core of the incoming fundamental instability. On the other hand,

in step case III, the streamwise evolution of $\hat{E}_\tau$ and $\hat{E}_{(0,1)}$ diverge at $x_{st}/\delta_0 \approx 8$. In Fig. 15, this streamwise position corresponds approximately to the location where the near-wall sub-harmonic content has significantly amplified in x and the strongest peak in the shape function profile begins to shift upward. We note that $x_{st}/\delta_0 \approx 8$ corresponds as well to the location where the amplitude decay of the fundamental instability (considering $\hat{E}_{(0,1)}$) decelerates in x. Immediately downstream, it starts to display growth again. We do not have conclusive evidence to justify whether this is mainly attributed to weakening of the mechanism which initially stabilizes the incoming primary instability or it is a consequence of sub-harmonic non-linear interactions.

V. Conclusion

We studied the effect of forward-facing steps of several heights to a pre-existing stationary crossflow instability in an incompressible swept-wing boundary layer. We performed Direct Numerical Simulations (DNS) of the laminar base flow and the stationary solution that arises from the interaction between the incoming instability and the step. The stationary primary crossflow mode is imposed at the inflow. The swept-wing flow is modeled as flow over a flat plate with a prescribed airfoil-like favourable pressure gradient obtained from independent experimental data on a 45° swept wing. The computational domain is swept and aligned with the leading edge of the wing. All steps are virtually located at 20% of the chord of the wing model. We performed DNS for three step heights and a smooth no-step case. A common inflow perturbation amplitude is imposed in all cases. The primary crossflow instability undergoes exponential growth until (at least) the virtual location of the step in the smooth case, as also predicted by linear stability methods applied to the computed base flow.

The analysis is restricted to the near-step regime. We contribute to the discussion in the literature with regard to the role played by main step-induced flow features in altering the development of the incoming perturbation upon interaction. Special emphasis was put on understanding the impact of the step on the primary crossflow disturbance itself, neglecting unsteady perturbation effects, since it remains an open problem in the literature. Accordingly, unsteady disturbances, which are an essential part of the transition mechanisms responsible for turbulent breakdown, were not triggered in the DNS. We assessed relevant stationary perturbation mechanisms at the step. We qualitatively and quantitatively characterized the modulation of the fundamental stationary crossflow disturbance upon interaction with the step, as well as the evolution of the sub-harmonics instability waves. Moreover, we identified and described the behaviour of secondary stationary perturbation structures. The study presented in this work sets the foundations for future investigations which will deepen on laminar-turbulent transition in swept wings due to forward-facing steps.

The topology of the base flow is significantly distorted by the presence of the step. We measured reversal of the base-flow velocity in the direction of the flat-plate, x, upstream of the step in all configurations. A second region of flow recirculation is captured downstream of the step, only in the two largest step cases. The values of peak reversed-flow do not exceed the local free-stream velocity by more than 3.3% in any case. Reversal of the crossflow component is induced upstream and downstream of the step as well, which is accompanied by secondary near-wall inflection points in the crossflow component.

We Fourier transformed the perturbation field in the spanwise direction. At the vicinity of the step, the fundamental Fourier mode contains (at least) two main perturbation structures. On the one hand, the primary stationary crossflow disturbance. When the step is approached in x, it lifts up and passes over it. We found that the incoming primary disturbance becomes amplified immediately upstream of the step; the larger the height of the step, the larger the amplitude difference with respect to the smooth case at the location of the step. On the other hand, we captured spanwise-alternating perturbation streaks induced immediately upstream of the step, close to the wall.

Downstream of the step, near-wall perturbation streaks develop as well. They are linked to a secondary peak in the perturbation shape function. This is a topological feature that we captured in all step cases and it manifests for all x immediately downstream of the step. The secondary peak is weak in the small step case. On the contrary, for the case of the largest step, the secondary peak attains amplitude values significantly larger than the original primary peak close to the step corner. Secondary perturbation structures in the form of spanwise-distributed vortices which counter-rotate with respect to each other accompany the system of streaks. They were identified in all step configurations. Sufficiently downstream of the step in the largest step case, primary and prominent secondary vortical structures eventually merge. We indicated that the secondary peak in the shape function of the fundamental Fourier mode, the near-wall system of streaks, and secondary perturbation vortices are manifestations of a common mechanism arising at the step.

For all step configurations, activity of the sub-harmonic disturbance content is enhanced downstream of the step. This feature is particularly prominent in the largest step case. The similarities between the behaviour of secondary peaks in the shape function of the fundamental and the high-order Fourier modes points towards the existence of a

common mechanism responsible for sudden near-wall perturbation growth at the step corner among different spanwise wavenumbers. Based on similarities with previous work, this may be ascribed to either transient growth [29] or to the effect of the upstream crossflow reversal [27]. We indicated strong correlation between the spatial location of secondary peaks in the perturbation shape and the location of step-induced inflection points in the crossflow component downstream of the step. When considering the fundamental Fourier mode, growth of secondary perturbation structures downstream of the step was only captured in the step-corner region. However, when considering the sub-harmonic instability waves in the largest step case, the perturbation growth initiated at the step corner is significantly enhanced further downstream, close to the location of the near-wall inflection points. This is not the case for the smallest step.

We introduced metrics to quantify the impact of the step on the evolution of the primary incoming crossflow disturbance upon interaction. To segregate secondary perturbation effects downstream of the step, we proposed to characterize amplitude at the wall-normal location of the primary peak in the shape function profile, which is associated to the core of the incoming disturbance. When this methodology is applied, we found that different perturbation-velocity components display significantly different streamwise growth rates. By using a definition of disturbance kinetic energy we reported that, for the smallest step cases, the primary crossflow instability grows monotonically at a rather constant rate downstream of the step. Interestingly, for our largest step, the incoming primary disturbance is strongly stabilized immediately downstream of the step. Significant growth of the sub-harmonic disturbance content was measured close to the streamwise position at which the primary crossflow perturbation grows again in x.

Appendix

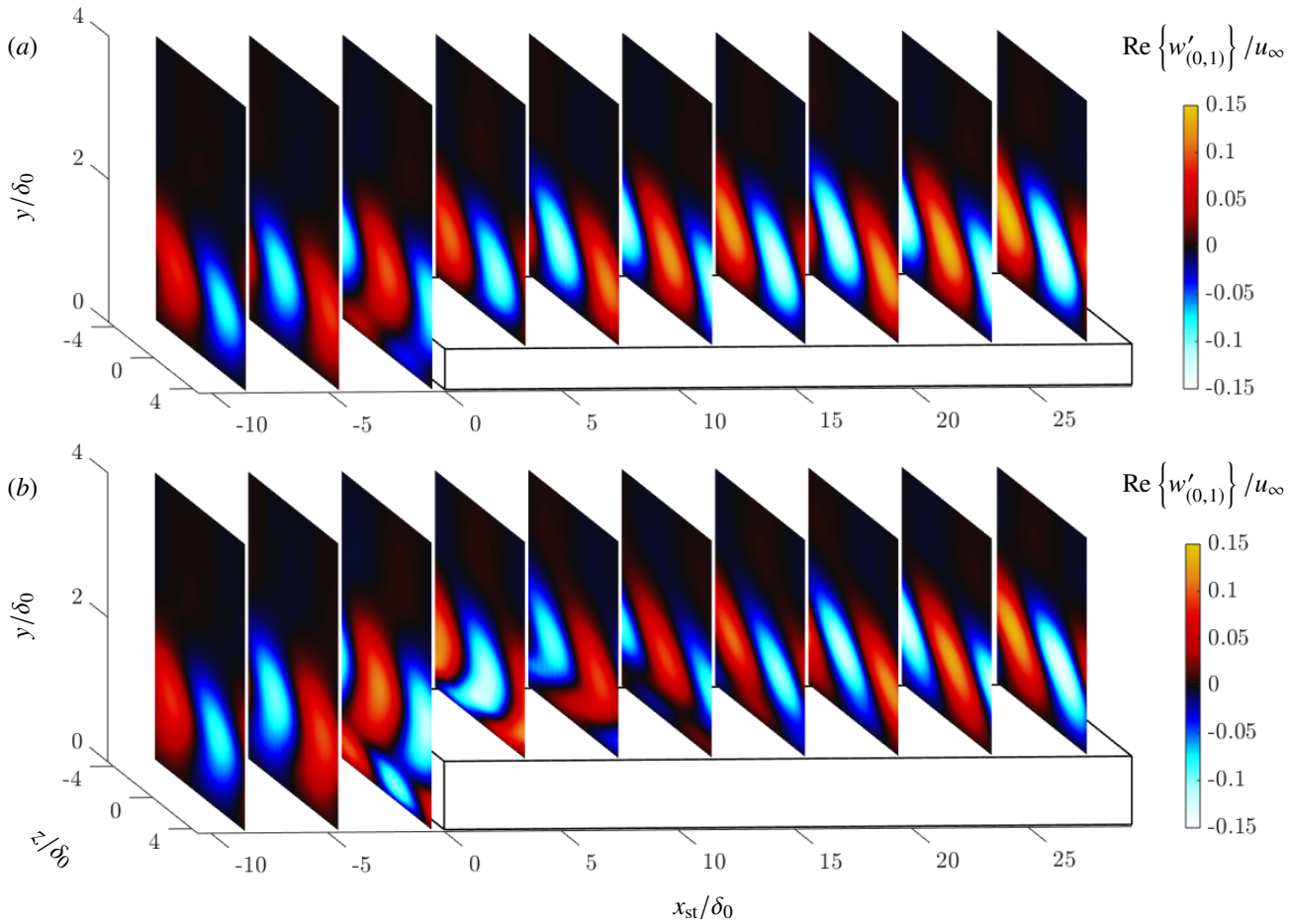

Figure 22 Three-dimensional organization of the spanwise-velocity-perturbation Fourier Mode $(0,1)$ at the step location for step cases I (*a*) and III (*b*).

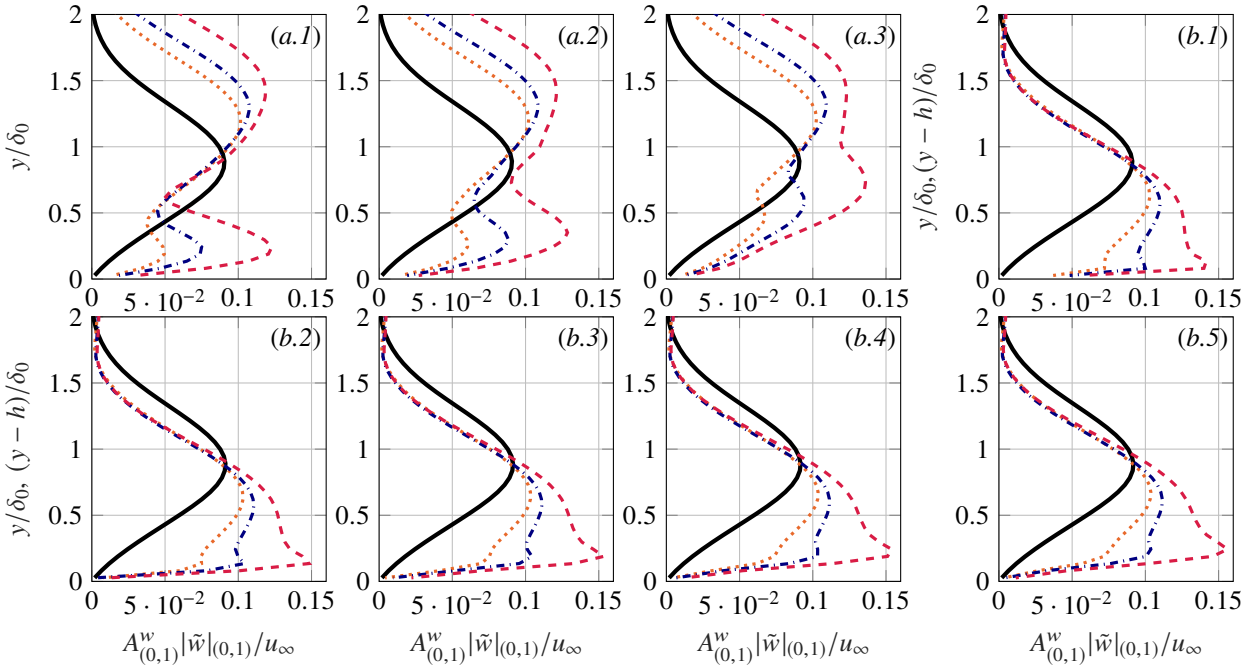

Figure 23 Profiles of $|\tilde{w}|_{(0,1)}$ at $x_{st}/\delta_0 = -0.32$ (*a.1*), -0.16 (*a.2*), -0.05 (*a.3*), 0.11 (*b.1*), 0.22 (*b.2*), 0.38 (*b.3*), 0.54 (*b.4*), 0.65 (*b.5*). Clean case (solid black), step case I (dotted orange), II (dash-dotted blue), III (dashed red).

Acknowledgments

This work was carried out on the Dutch national e-infrastructure with the support of SURF Cooperative. J. C. Author thanks Dr. Koen J. Groot, Dr. Theodoros Michelis, and Haris Shahzad for the fruitful discussions, as well as his *corona family* for the support during the global pandemic of covid-19.

References

[1] Perraud, J., and Séraudie, A., "Effects of steps and gaps on 2D and 3D transition," *European Congress on Computational Methods in Applied Sciences and Engineering*, ECCOMAS, Barcelona, Spain, 2000.

[2] Tufts, M. W., Reed, H. L., Crawford, B. K., Duncan Jr., G. T., and Saric, W. S., "Computational investigation of step excrescence sensitivity in a swept-wing boundary layer," *J. Aircr.*, Vol. 54, 2017.

[3] Rius-Vidales, A. F., Kotsonis, M., Antunes, A., and Cosin, R., "Effect of two-dimensional surface irregularities on swept wing transition: forward facing steps," *AIAA Paper 2018-3075*, 2018.

[4] Drake, A., Bender, A., Korntheuer, A., Westphal, R. V., McKeon, B. J., Gerashchenko, S., Rohe, W., , and Dale, G., "Step excrescence effects for manufacturing tolerances on laminar flow wings," *AIAA Paper 2010-375*, 2010.

[5] Duncan Jr., G. T., Crawford, B. K., Tufts, M. W., Saric, W. S., and Reed, H. L., "Effects of step excrescences on swept-wing transition," *AIAA Paper 2013-2412*, 2013.

[6] Duncan Jr., G. T., Crawford, B. K., Tufts, M. W., Saric, W. S., and Reed, H. L., "Effects of step excrescence on a swept wing in a low-disturbance wind tunnel," *AIAA Paper 2014-0910*, 2014.

[7] Saeed, T. I., Mughal, M. S., and Morrison, J. F., "The interaction of a swept-wing boundary layer with surface excrescences," *AIAA Paper 2016-2065*, 2016.

[8] Eppink, J. L., and Casper, C., "Effects of forward-facing step shape on stationary crossflow instability growth and breakdown," *AIAA Paper 2019-3532*, 2019.

[9] Sumariva, J. A. F., and Hein, S., "Adaptive harmonic linearized Navier-Stokes equations used for boundary-layer instability analysis in the presence of large streamwise gradients," *AIAA Paper 2018-1548*, 2018.

[10] Cooke, E. E., Mughal, S., Sherwin, S. J., Ashworth, R., and Rolston, S., "Destabilization of stationary and traveling crossflow disturbances due to steps over a swept wing," *AIAA Paper 2019-3533*, 2019. https://doi.org/10.2514/6.2016-3690.

[11] Bippes, H., "Basic experiments on transition in the three-dimensional boundary layers dominated by crossflow instability," *Prog. Aerosp. Sci.*, Vol. 35, 1999, pp. 363–412.

[12] Saric, W. S., Reed, H. L., and White, E. B., "Stability and transition of three-dimensional boundary layer," *Annu. Rev. Fluid Mech.*, Vol. 35, 2003, pp. 413–40.

[13] Wassermann, P., and Kloker, M., "Mechanisms and passive control of crossflow-vortex-induced transition in a three-dimensional boundary layer," *J. Fluid Mech.*, Vol. 456, 2002, pp. 49–84.

[14] Hosseinverdi, S., and Fasel, H. F., "Direct Numerical Simulations of laminar-to-lurbulent lransition in laminar leparation lubbles in lhree-limensional loundary-layer," *AIAA Paper 2016-3793*, 2016.

[15] Schmid, P. J., and Henningson, D. S., *Stability and transition in shear flows*, Vol. 142, Springer, 2001.

[16] Hickel, S., Egerer, C. P., and Larsson, J., "Subgrid-scale modeling for implicit large eddy simulation of compressible flows and shock-turbulence interaction," *Phys. Fluids*, Vol. 26, 2014, pp. 106–101.

[17] Hickel, S., and Adams, N. A., "Implicit LES applied to zero-pressure-gradient and adverse-pressure-gradient boundary-layer turbulence," *Int. J. Heat Fluid Fl.*, Vol. 29, 2008, pp. 626–639.

[18] Hu, W., Hickel, S., and van Oudheusden, B., "Dynamics of a supersonic transitional flow over a backward-facing step," *Phys. Rev. Fluid*, Vol. 4, 2019.

[19] Casacuberta, J., Groot, K. J., Ye, Q., and Hickel, S., "Transitional flow dynamics behind a micro-ramp," *Flow Turbul. Combust.*, Vol. 104, 2019, pp. 533–552.

[20] Bertolotti, F. P., Herbert, T., and Spalart, P. R., "Linear and nonlinear stability of the Blasius boundary layer," *J. Fluid Mech.*, Vol. 242, 1992, pp. 441–474.

[21] Rodríguez, D., Gennaro, E., and Juniper, M., "The two classes of primary modal instability in laminar separation bubbles," *J. Fluid Mech.*, Vol. 734, 2013. https://doi.org/10.1017/jfm.2013.504.

[22] Alam, M., and Sandham, N., "Direct Numerical Simulation of 'short' laminar separation bubbles with turbulent reattachment," *J. Fluid Mech.*, Vol. 410, 2000, pp. 1–28.

[23] Eppink, J. L., "Mechanisms of stationary cross-flow instability growth and breakdown induced by forward-facing steps," *J. Fluid Mech.*, Vol. 897, 2020, p. A15.

[24] Hunt, J., Wray, A., and Moin, P., "Eddies, streams, and convergence zones in turbulent flows," Report CTR-S88, center for turbulence research, 1988.

[25] Marxen, O., Lang, M., Rist, U., Levin, O., and Henningson, D. S., "Mechanisms for spatial steady three-dimensional disturbance growth in a non-parallel and separating boundary layer," *J. Fluid Mech.*, Vol. 634, 2009, pp. 165–189.

[26] Jeong, J., and Hussain, F., "On the identification of a vortex," *J. Fluid Mech.*, Vol. 285, 1995, pp. 69–94.

[27] Eppink, J. L., "The effect of forward-facing steps on stationary crossflow instability growth and breakdown," *AIAA Paper 2018-0817*, 2018.

[28] Blackburn, H. M., Barkley, D., and Sherwin, S. J., "Convective instability and transient growth in flow over a backwar-facing step," *J. Fluid Mech.*, Vol. 603, 2008, pp. 271–304.

[29] Lanzerstorfer, D., and Kuhlmann, H. C., "Three-dimensional instability of the flow over a forward-facing step," *J. Fluid Mech.*, Vol. 695, 2012, pp. 390–404.

[30] Breuer, K. S., and Kuraishi, T., "Transient growth in two- and three-dimensional boundary layers," *Phys. Fluids*, Vol. 6, 1998.